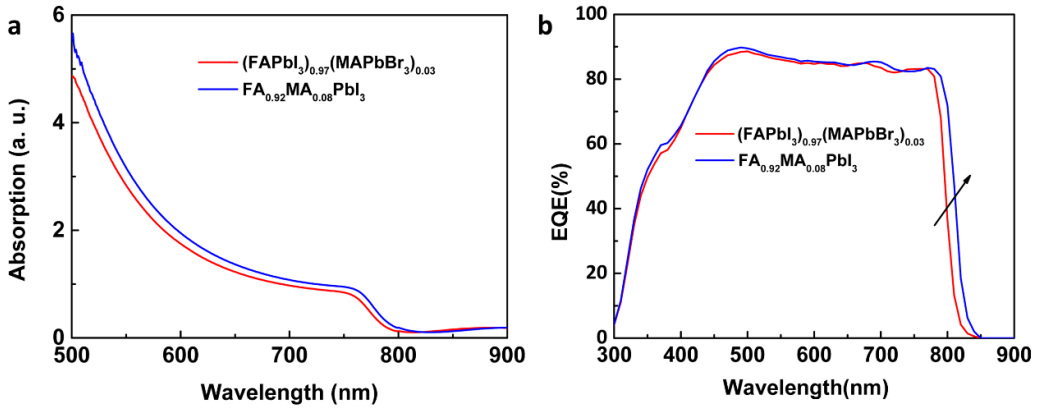


In the format provided by the authors and unedited.

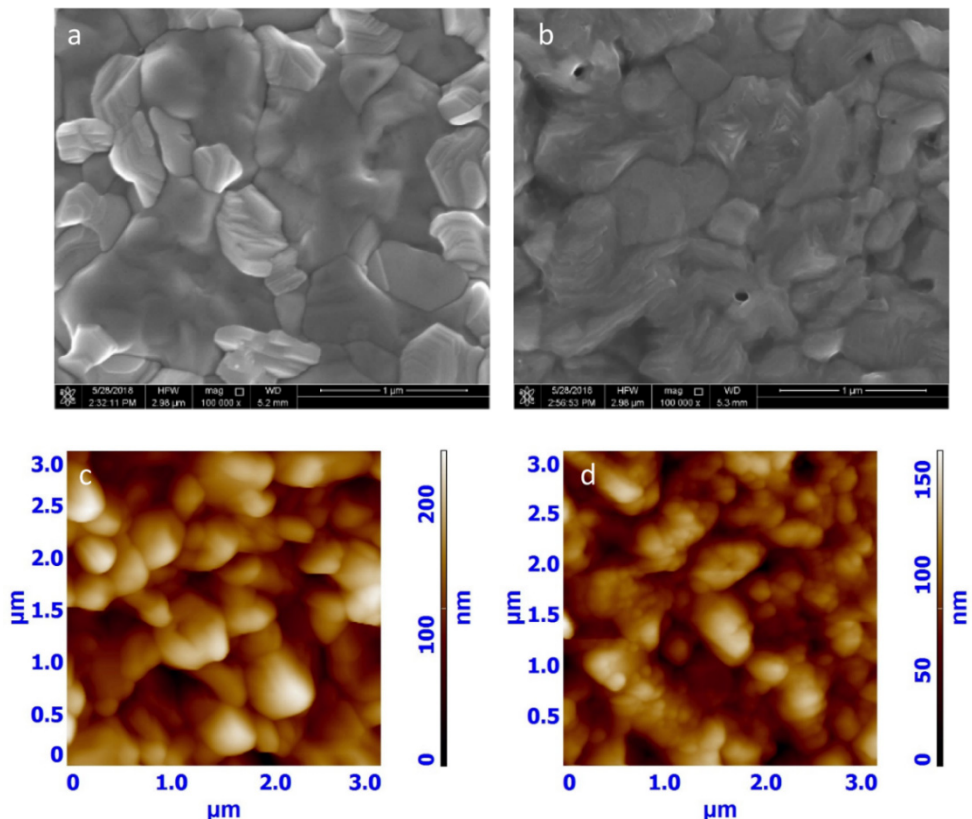
Surface passivation of perovskite film for efficient solar cells

Qi Jiang^{1,2}, Yang Zhao^{1,2}, Xingwang Zhang^{ID 1,2}, Xiaolei Yang¹, Yong Chen^{1,2}, Zema Chu^{1,2}, Qiufeng Ye^{1,2}, Xingxing Li^{1,2}, Zhigang Yin^{1,2} and Jingbi You^{ID 1,2*}

¹Key Laboratory of Semiconductor Materials Science, Institute of Semiconductors, Chinese Academy of Sciences, Beijing, China. ²Center of Materials Science and Optoelectronics Engineering, University of Chinese Academy of Sciences, Beijing, China. *e-mail: jyou@semi.ac.cn

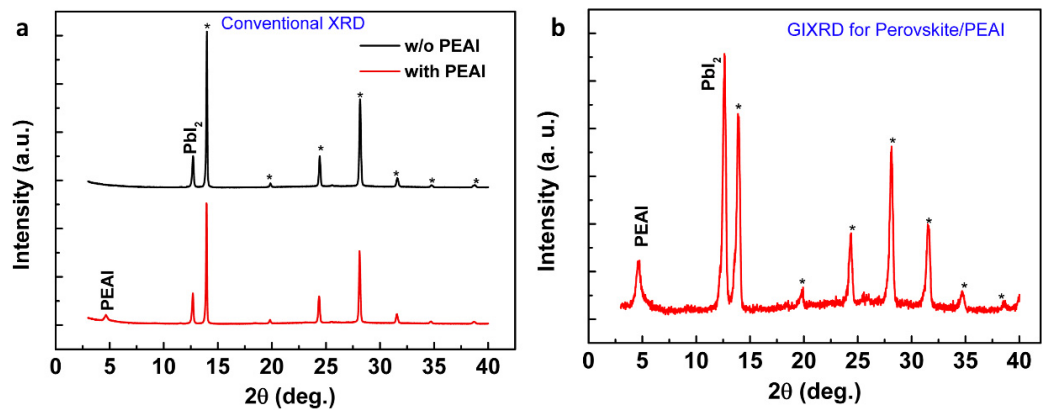


Supplementary Fig.1| a, Ultraviolet-visible absorption of $(\text{FAPbI}_3)_{0.97}(\text{MAPbBr}_3)_{0.03}$ and $\text{FA}_{0.92}\text{MA}_{0.08}\text{PbI}_3$. **b,** The external quantum efficiency (EQE) of the solar cells using $(\text{FAPbI}_3)_{0.97}(\text{MAPbBr}_3)_{0.03}$ and $\text{FA}_{0.92}\text{MA}_{0.08}\text{PbI}_3$ as absorber layer by using the structure of ITO/SnO₂/perovskite/Spiro-OMeTAD/Au. Both of the absorption and external quantum efficiency have been redshift while replacing MABr by MAI in FAPbI₃.

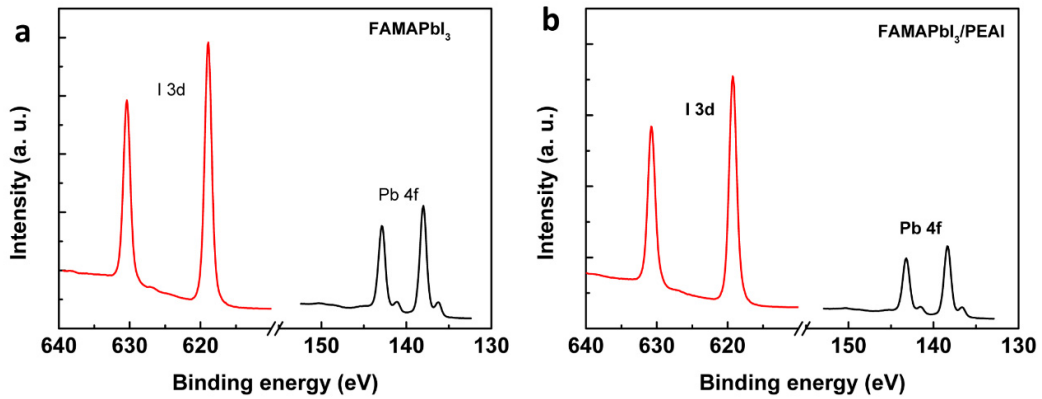


Supplementary Fig. 2| Morphology of perovskite film with and without PEAi treatment.

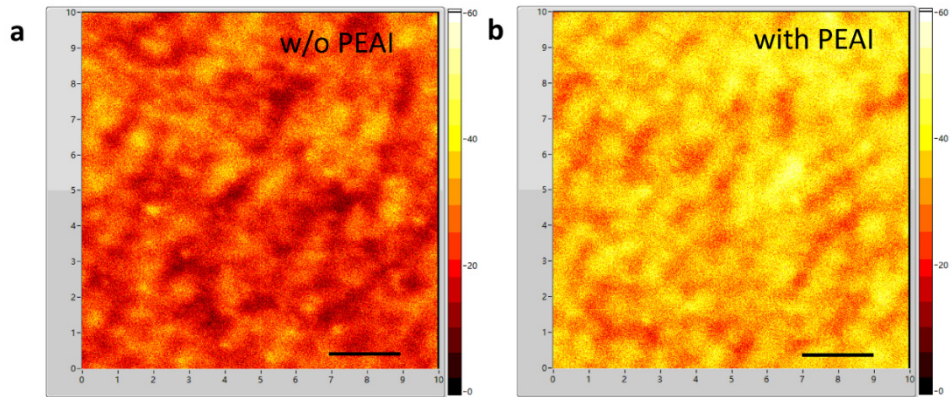
a and **b**, Scanning electron microscopy (SEM) images of perovskite films without and with PEAi coating, respectively. **c** and **d**, Atomic force microscopy (AFM) images of perovskite films without and with PEAi coating, respectively. For the control perovskite films without PEAi treatment, as similar as our previous reports^{8,25}, there are two separated phases. The dark grain region is perovskite crystal, and the white grains surrounding perovskite phase are PbI₂^{8,25}. After PEAi coating, the PbI₂ layer has been fully covered as we can Supplementary Fig. 3b. The roughness of perovskite layer has been reduced from 32 to 24 nm after PEAi coating, indicates that PEAi salt are more easily deposited at grain boundary (usually, there is a valley at grain boundary, Supplementary Fig. 7), and thus reduces the height difference between the grain surface and grain boundary.



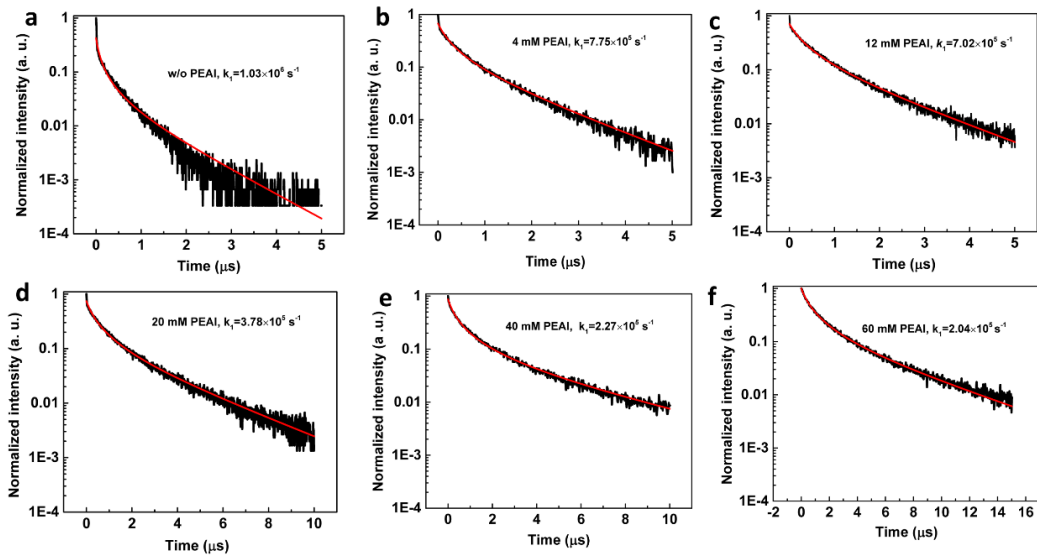
Supplementary Fig. 3| a, Conventional X-ray (θ - 2θ model) diffraction patterns of perovskite with and without PEAI layer. **b**, Grazing incident X-ray diffraction of perovskite with PEAI layer, the incident angle is 0.5° .



Supplementary Fig. 4| Pb 4f and I 3d core energy level spectra from FAMAPbI₃ without **(a)** and with **(b)** phenethylammonium iodide (PEAI) coating. It can be estimated that the ratio of Pb/I are 1:1.55 and 1:2.34 for perovskite film without and with PEAI coating, respectively, indicating that the iodine amount at surface has been significantly increased, which could reduce the iodine vacancies defects on the surface.



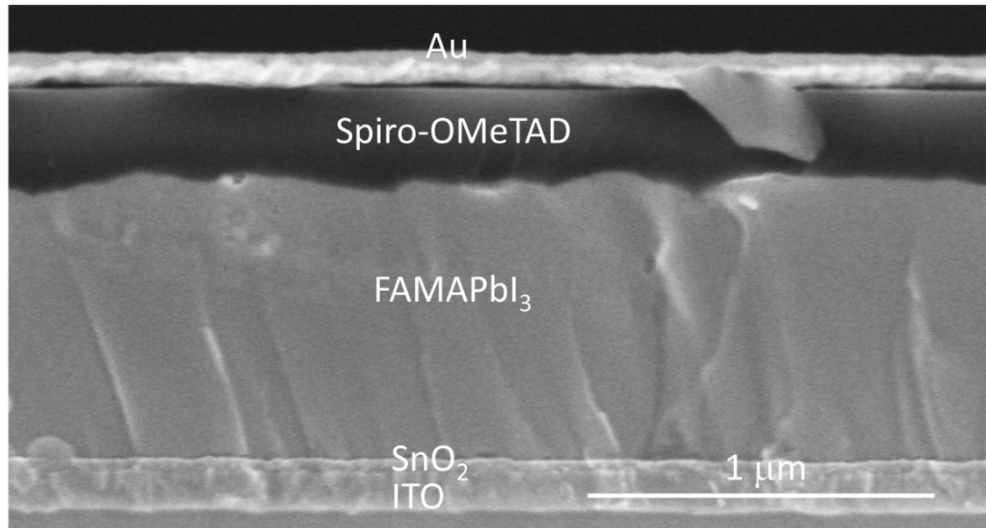
Supplementary Fig. 5| a and b, The photoluminescence mapping of perovskite films without and with PEA treatment, respectively, the excitation wavelength is 470 nm.



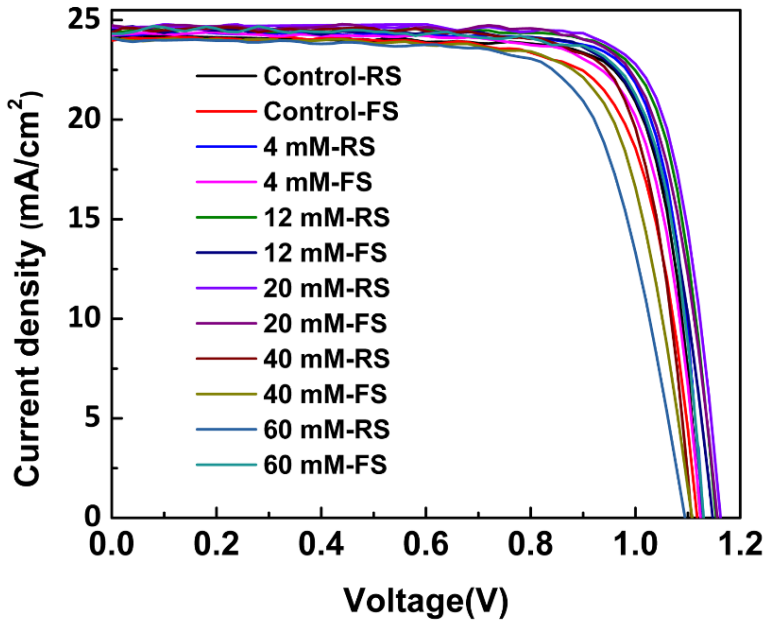
Supplementary Fig. 6| Fitting of the time resolved photoluminescence (TRPL) of the perovskite films coated with different concentrations of PEAI. The charge carrier lifetime was obtained by fitting TRPL results, while we also quantitatively the charge carrier recombination in the perovskite films from PL decay results, the kinetics of charge carrier recombination can be established by the differential rate law: $-dn/dt=k_1n+k_2n^2$, k_1 and k_2 represent the first and second order rate constants for non-radiative and bimolecular radiative recombination of charge carriers, respectively⁴⁰. The lifetime and non-radiative recombination rate are summarized in Extend Data Table 1.

Supplementary Table 1. Summary of the life time and non-radiative recombination rate for the perovskite films with different concentrations of PEAI solution treatment.

PEAI Concentration	W/O	4 mM	12 mM	20 mM	40 mM	60 mM
Lifetime (ns)	364	760	881	1430	2099	2835
$k_1(10^5 \text{ s}^{-1})$	10.3	7.75	7.02	3.78	2.27	2.04



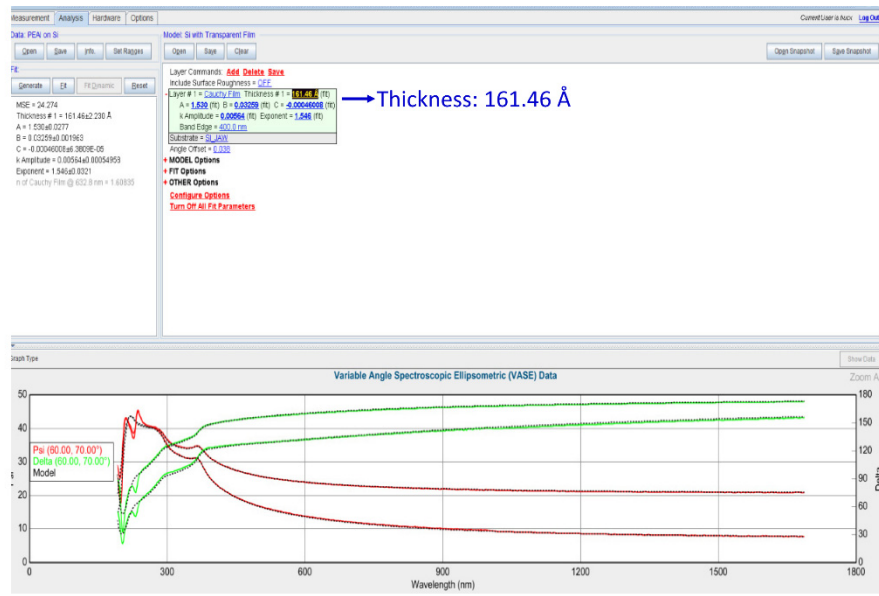
Supplementary Fig. 7| Scanning electron microscopy (SEM) image of the completed devices, *i.e.* glass/ITO/SnO₂/FAMAPbI₃/Spiro-OMeTAD/Au. The thicknesses of SnO₂, FAMAPbI₃, Spiro-OMeTAD are about 40 nm, 800 nm and 250 nm, respectively.



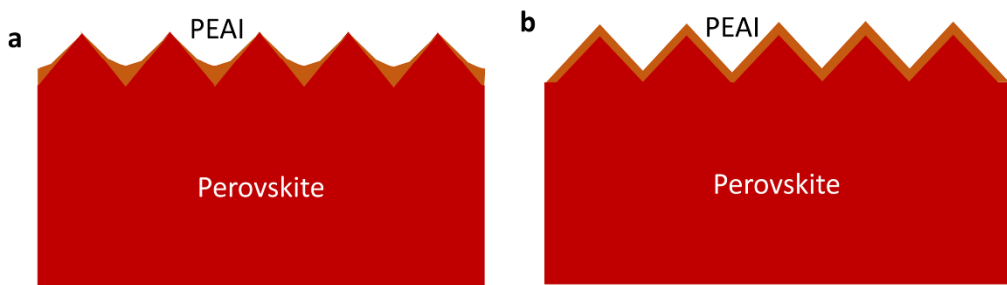
Supplementary Fig. 8| Device performance with different concentration of PEAI treatment. The J-V curve of the devices with different concentrations of PEAI treatment ranging from 0 mM to 60 mM, and the J-V curve from reverse scan (1.2 V to 0 V) and forward scan (0 V to 1.2 V) are both collected.

Supplementary Table 2| Summary of the device performance with different concentrations of PEAI treatment, H-index define as: $H\text{-index} = (\text{PCE}_{\text{reverse}} - \text{PCE}_{\text{Forward}})/\text{PCE}_{\text{Reverse}}$. $\text{PCE}_{\text{reverse}}$ and $\text{PCE}_{\text{forward}}$ are the power conversion efficiency from reverse and forward scan, respectively.

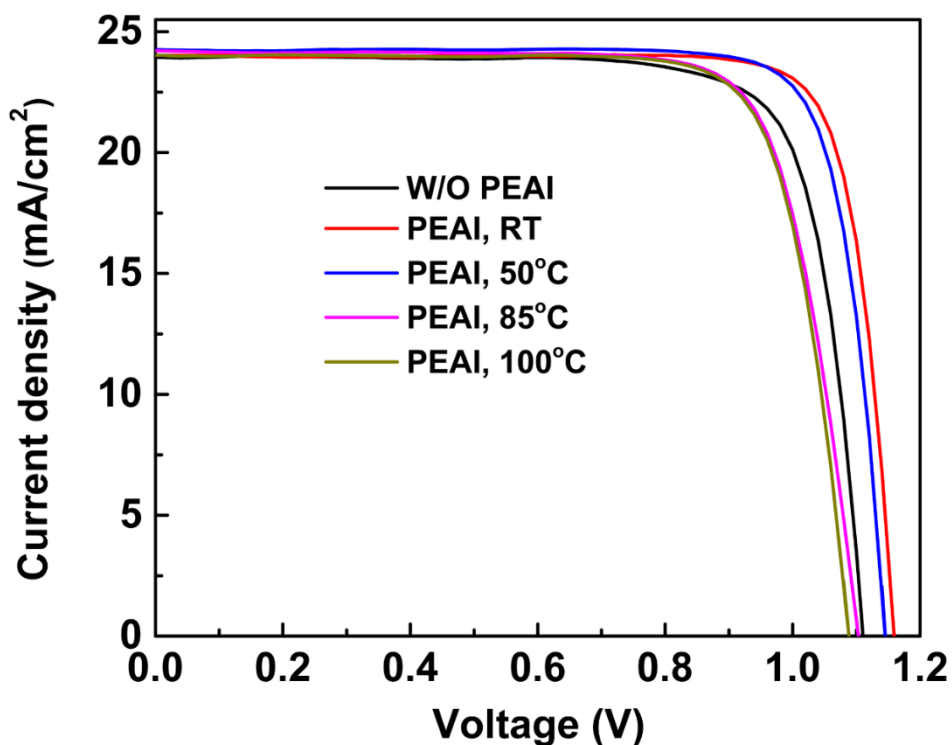
PEAI Concentration	Scan Direction	V _{oc} (V)	J _{sc} (mA/cm ²)	FF (%)	PCE (%)	Average	H-index
Control	RS	1.12	24.25	79.12	21.48	20.89%	5.44%
	FS	1.12	23.98	75.64	20.31		
4 mM	RS	1.13	24.24	80.99	22.18	21.62%	5.04%
	FS	1.12	24.25	77.54	21.06		
12 mM	RS	1.15	24.49	79.91	22.50	22.12%	3.37%
	FS	1.15	24.49	77.20	21.74		
20 mM	RS	1.16	24.64	79.60	22.75	22.60%	1.36%
	FS	1.16	24.73	78.24	22.44		
40 mM	RS	1.11	24.59	78.27	21.37	21.19%	1.73%
	FS	1.11	24.50	77.36	21.00		
60 mM	RS	1.11	24.11	74.54	19.95	19.48%	4.76%
	FS	1.09	24.10	72.33	19.00		



Supplementary Fig. 9| The thicknesses of PEA1 layer measured by ellipsometer. The concentration of PEA1 precursor film is 20 mM, and it was spin-coated on Si substrate, the mass thickness of PEA1 is about 16 nm. The thickness of PEA1 deposited on rough perovskite might be a little different (surely within a factor of 2) from that on the smooth substrate.



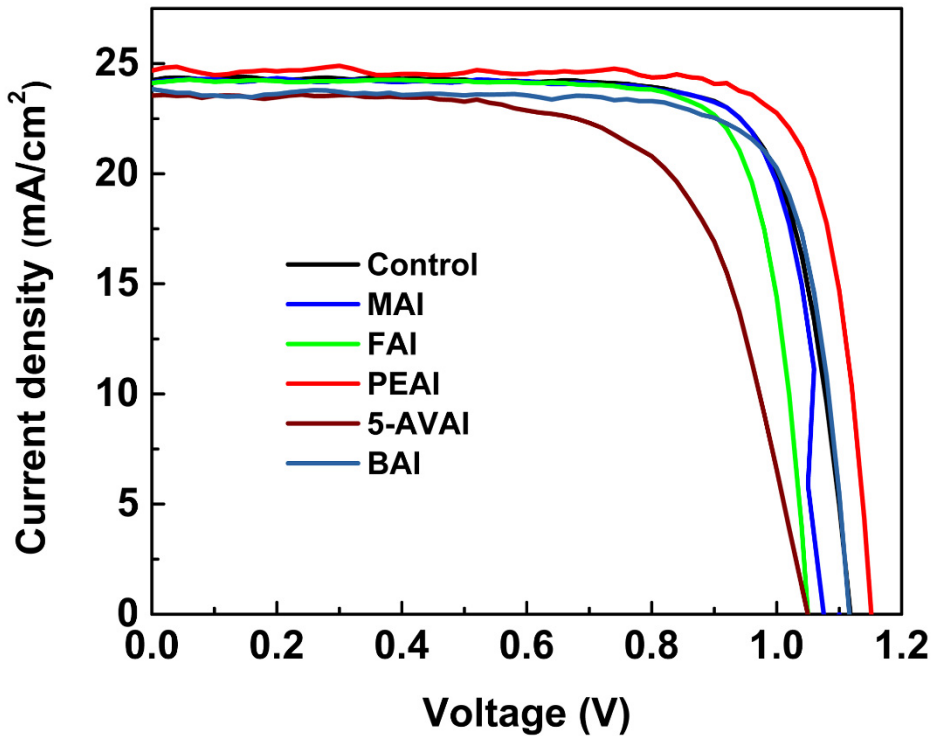
Supplementary Fig. 10| Two possible growth models while depositing PEA1 on perovskite surface. While depositing several ten nanometers PEA1 on very rough surface by solution process, case (a) will be happened, and the conformal growth such as case (b) could be impossible. In case of (a), PEA1 at some place are thin enough for charge transfer by tunneling, for some place with thick PEA1 layer, the charges could be drifted/diffused into adjacent places with thin PEA1 layer, and then transfer into hole transport layer.



Supplementary Fig. 11| The device performance while processing the PEAi layer under different conditions: without PEAi and with PEAi processed at different temperatures for 5 min.

Supplementary Table 3| Summary of the device performance while processing under different temperature.

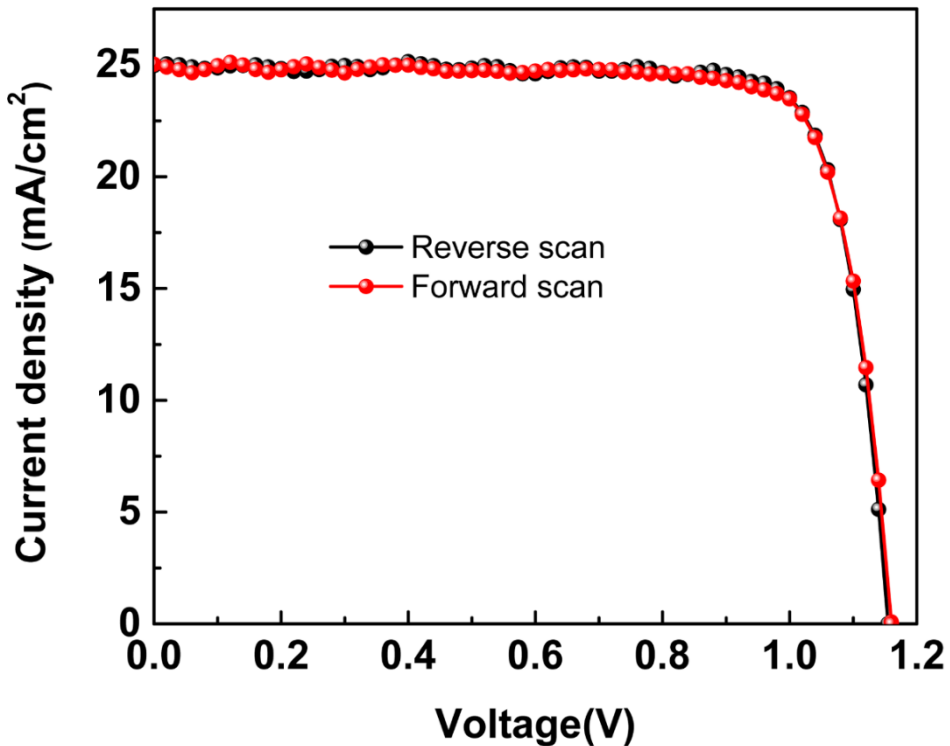
Perovskite/PEAI	V _{oc} (V)	J _{sc} (mA/cm ²)	FF (%)	PCE (%)
w/o PEAi	1.11	23.94	78.83	20.95
With PEAi, RT	1.16	24.02	82.92	23.10
With PEAi, 50°C	1.15	24.26	81.92	22.85
With PEAi, 85°C	1.10	24.22	77.62	20.68
With PEAi, 100°C,	1.09	24.03	78.45	20.55



Supplementary Fig. 12| Device performance while treating perovskite surface with different organic salts. Methylammonium iodide (MAI), Formamidinium iodide (FAI), phenethylammonium iodide (PEAI), 5-Ammonium valeric acid iodide (5-AVAI) and n-Butylammonium iodide (BAI). The reverse scan J-V are given.

Supplementary Table 4|. Summary of the device performance while treating perovskite surface with different organic salts.

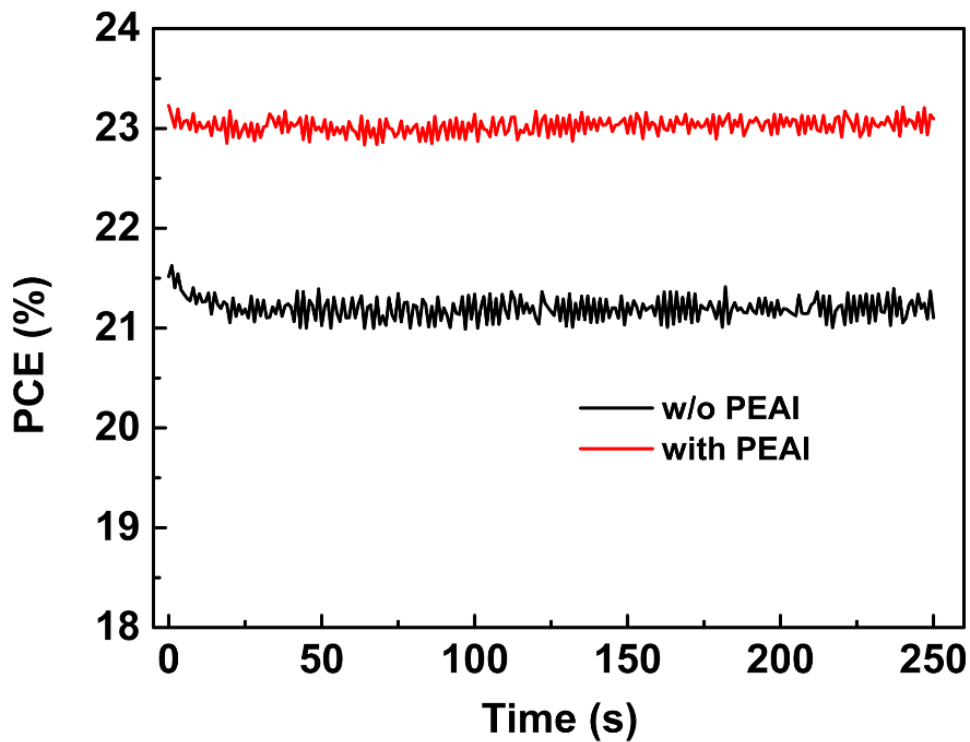
Perovskite/PEAI	V _{oc} (V)	J _{SC} (mA/cm ²)	FF (%)	PCE (%)
Perovskite	1.12	24.24	78.23	21.24
Perovskite/MAI	1.10	24.16	79.95	21.25
Perovskite/FAI	1.05	24.12	80.53	20.53
Perovskite/PEAI	1.15	24.69	80.06	22.73
Perovskite/5-AVAI	1.05	23.55	67.29	16.64
Perovskite/BAI	1.12	23.84	77.84	20.78



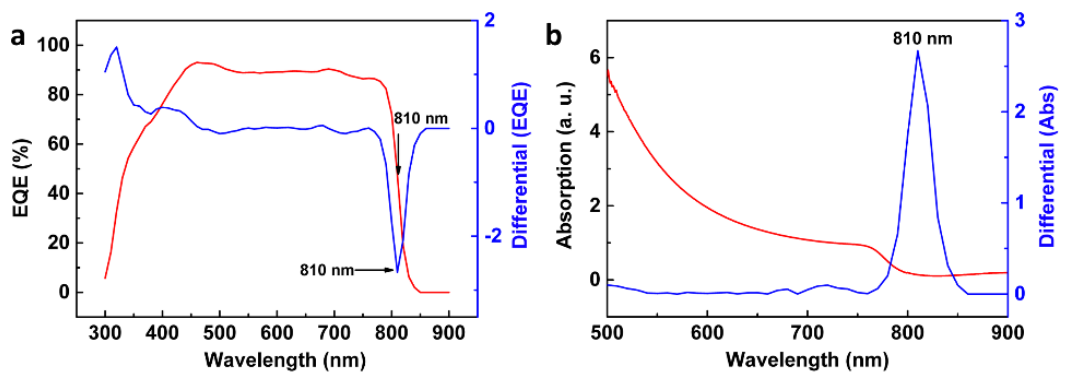
Supplementary Fig. 13| The J-V curve from the reverse scan (1.2 V to 0 V) and forward scan (0 V to 1.2 V) for the champion device under 1 Sun condition (100 mW/cm²).

Supplementary Table. 5| The device performance parameters for the champion device under reverse scan (1.2 V to 0V) and forward scan (0 V to 1.2 V).

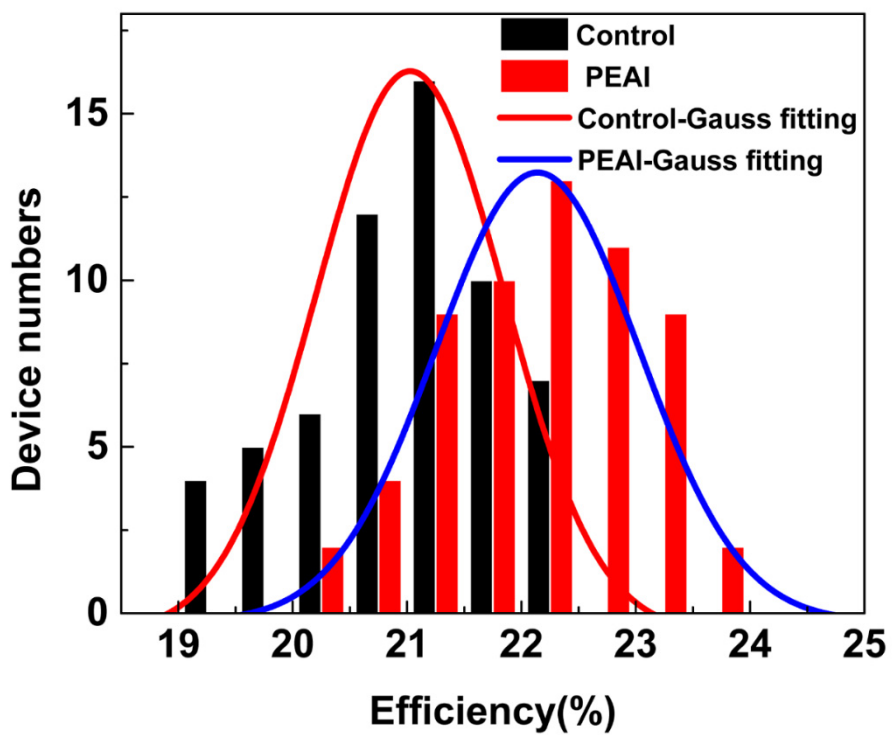
Scan direction	V _{oc} (V)	J _{sc} (mA/cm ²)	FF (%)	PCE (%)
Reverse	1.15	24.96	81.97	23.53
Forward	1.16	25.03	80.86	23.48



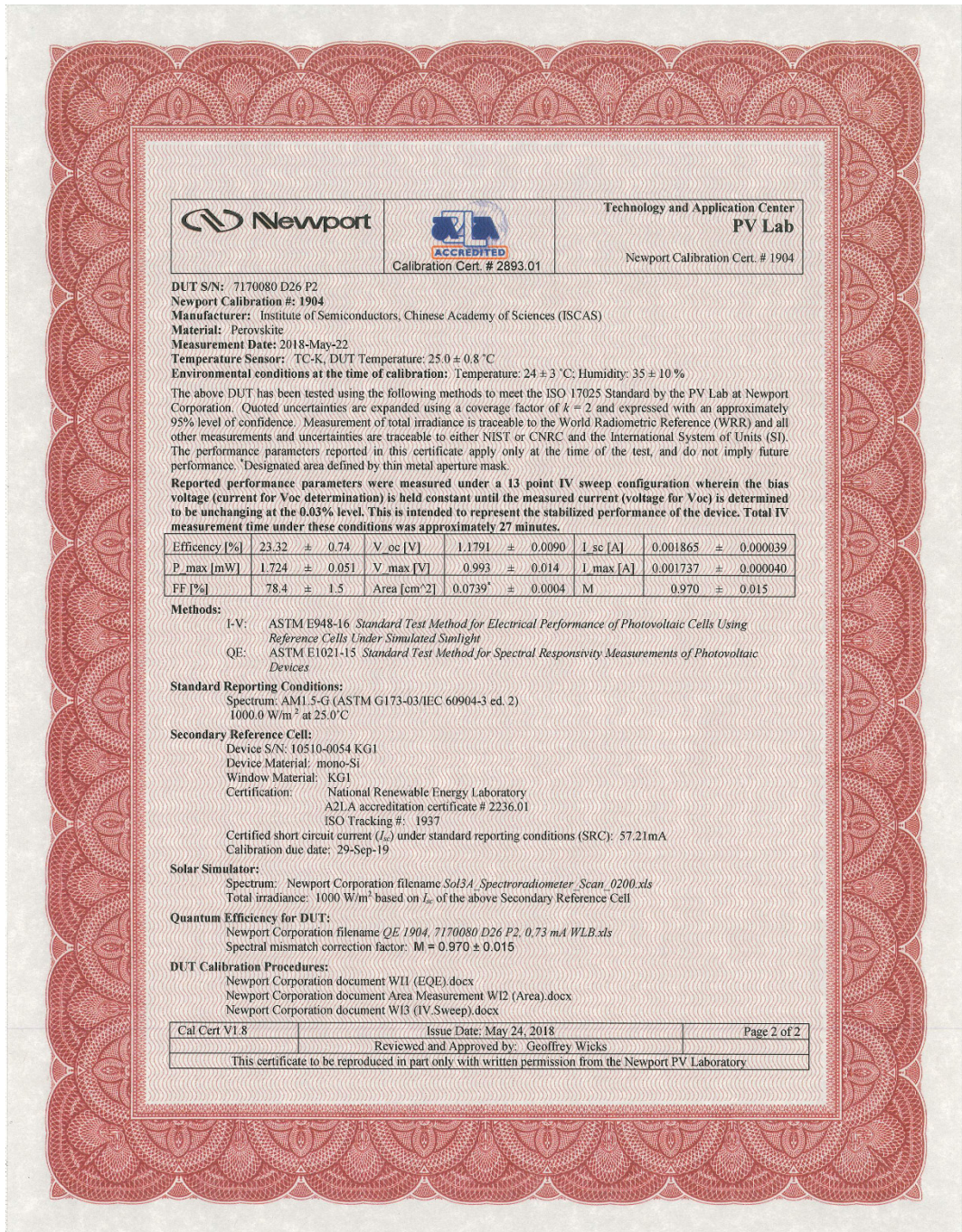
Supplementary Fig. 14| The steady-state power output for the control and also for the best device with PEAI layer. The maximum voltage for the devices without and with PEAI are 0.96 V and 0.99 V, respectively, the maximum current density are 22.2mA/cm^2 and 23.4mA/cm^2 , respectively, and the steady-state output for are 21.3% and 23.2% for control and PEAI treated devices, respectively.



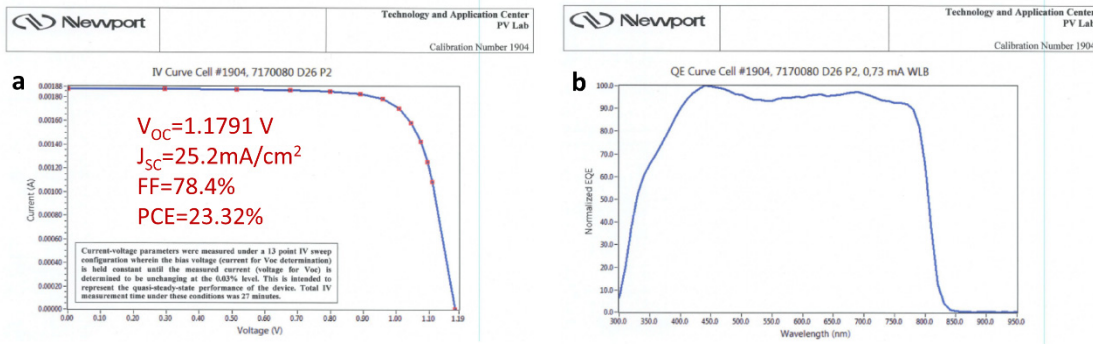
Supplementary Fig. 15| Three different methods to determine the absorption threshold of perovskite layer. **a**, EQE falls to half peak value method and differential of EQE. **b**, Differential of absorption.



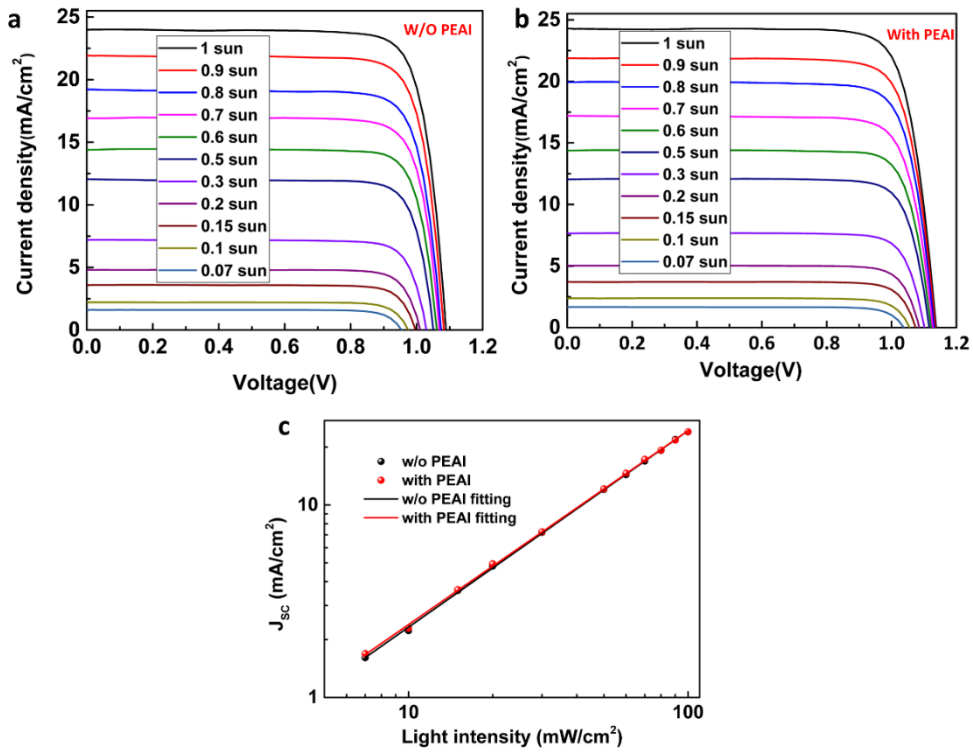
Supplementary Fig. 16| The device power conversion efficiency (PCE) distribution for the devices with and without PEAI treatment, 60 devices data are collected for each type of device.



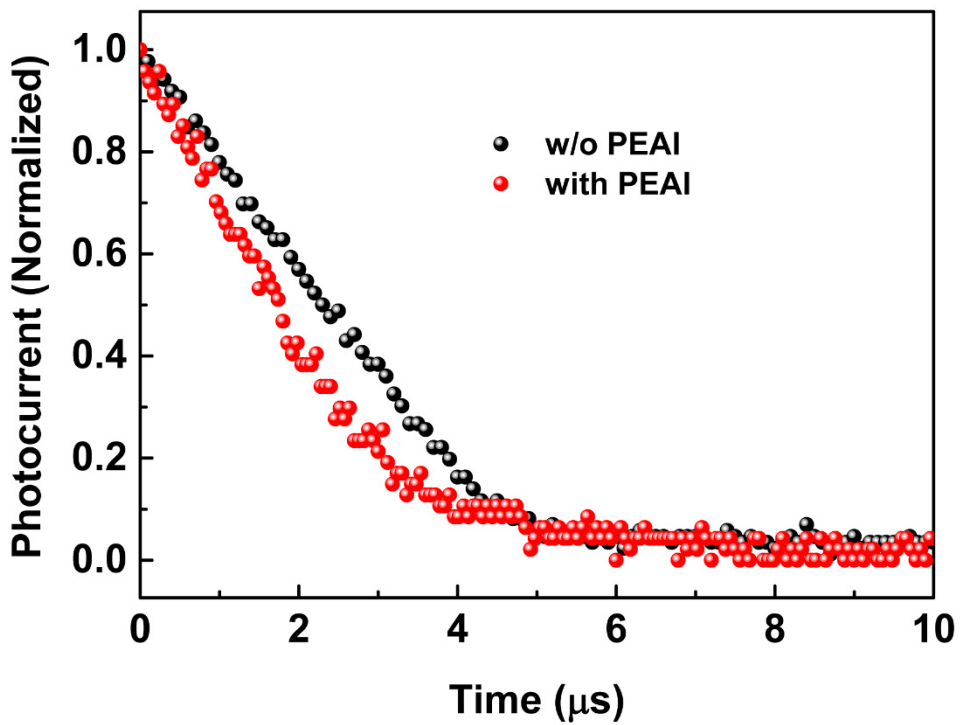
Supplementary Fig. 17| Certificated results from an accredited photovoltaic certification laboratory (Newport, USA). The certificated efficiency is 23.32%. Our devices area was 0.108 cm^2 , while certification, a mask with the area of 0.0739 cm^2 has been used.



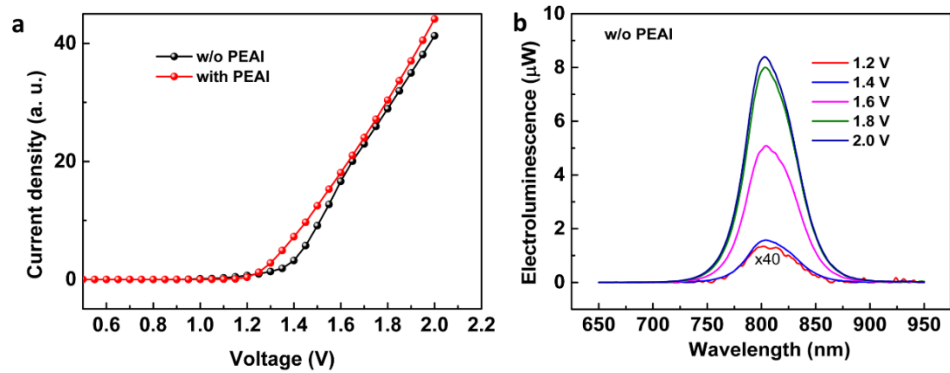
Supplementary Fig. 18| Certification results of perovskite solar cells at Newport, USA. **a**, Certificated J-V curve, the V_{OC} is 1.1791V, J_{SC} is 25.2 mA/cm², FF is 78.4% and the PCE is 23.32%. The current-voltage parameters were measured under a 13 point IV sweep configuration wherein the bias voltage (current for V_{OC} determination) is held constant until the measured current (voltage for V_{OC}) is determined to be unchanging at the 0.03% level. This is intended to represent the quasi-steady-state performance of the device. Total I-V measurement time under these condition was 27 min. **b**, Normalized external quantum efficiency (EQE) measured at Newport, under measurement, a white bias has been applied, the EQE has been used for spectra mismatch calculation.



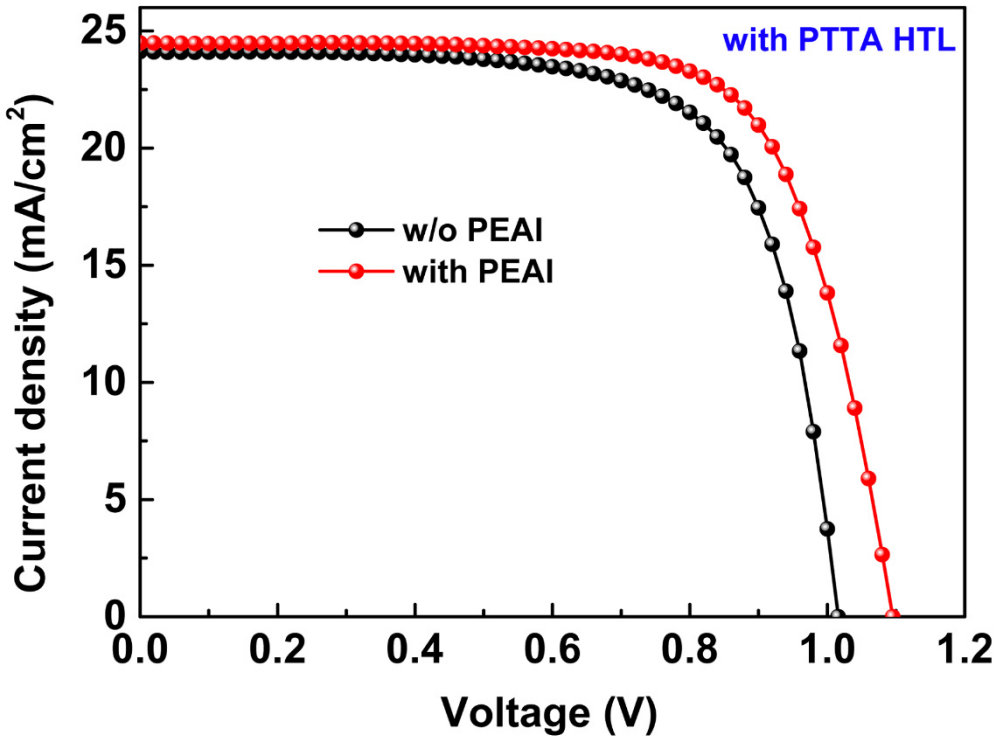
Supplementary Fig. 19| The response of solar cells under different light intensities for the control and PEAI-treated devices. **a**, J-V curve of the device without PEAI treatment under different light intensity ranging from 0.07 Sun to 1 Sun. **b**, J-V curve of the device with PEAI treatment under different light intensity ranging from 0.07 Sun to 1 Sun. **c**, The relationship between J_{sc} vs light intensity for the devices with and without PEAI treatment.



Supplementary Fig. 20| Transit photo-current (TPC) for the devices with and without PEAI treatment.



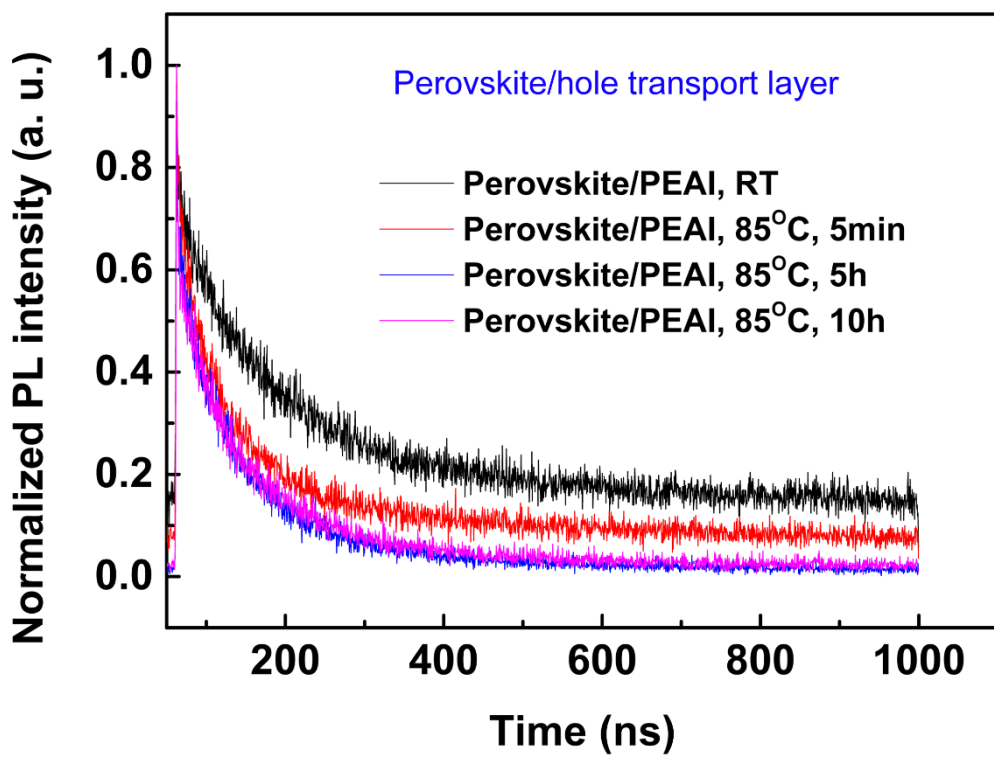
Supplementary Fig. 21| a, J-V curve of the devices with and without PEAI treatment under dark. **b**, The electroluminescence spectra of perovskite solar cells without PEAI treatment under different voltage bias in dark, the emission intensity at 1.2 V has been multiplied by 40.



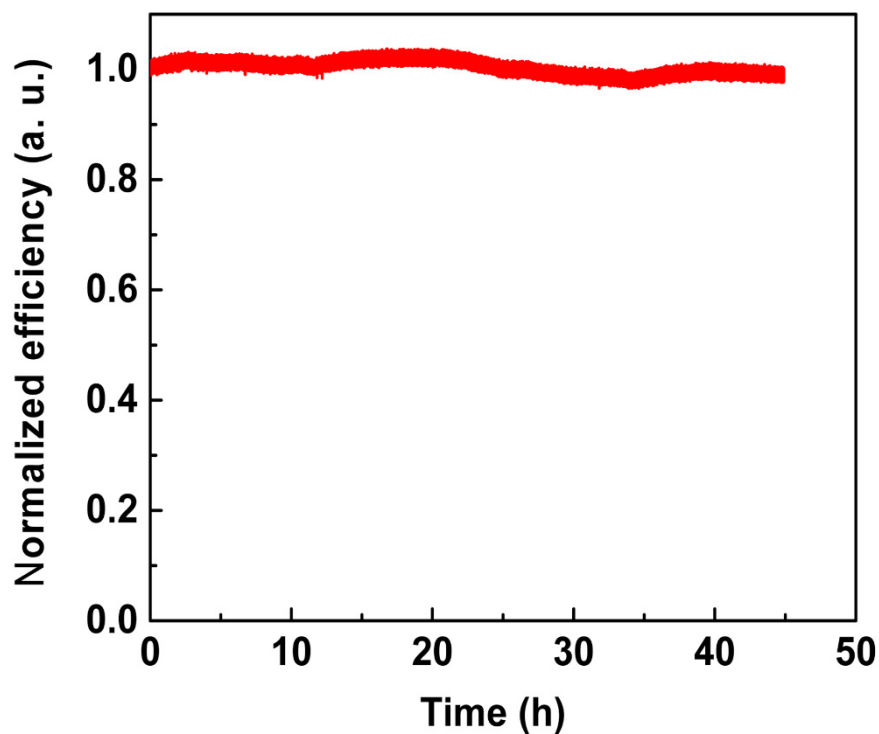
Supplementary Fig. 22| The initial current density-voltage (J-V) curve for the devices with and without PEA1 layer while using PTAA as the hole transport layer (HTL), these devices have been used for the thermal stressing test at 85°C.

Supplementary Table. 6| The device performance parameters of the devices for the thermal stressing test.

	V_{oc} (V)	J_{sc} (mA/cm^2)	FF (%)	PCE (%)
w/o PEA1	1.10	24.49	71.40	19.15
With PEA1	1.02	24.12	70.47	17.27



Supplementary Fig. 23| Time resolved photoluminescence of perovskite/PEAI with hole transport layer, where the perovskite/PEAI layer was annealed at 85°C for different time.



Supplementary Fig. 24|The device stability under continuous light soaking at maximum power point condition (measurement condition: 25°C, 100 mW/cm²), during measurement, a fan was put close to the device to keep the device temperature around 25°C.

Solar Cells Reporting Summary

Nature Research wishes to improve the reproducibility of the work that we publish. This form is intended for publication with all accepted papers reporting the characterization of photovoltaic devices and provides structure for consistency and transparency in reporting. Some list items might not apply to an individual manuscript, but all fields must be completed for clarity.

For further information on Nature Research policies, including our [data availability policy](#), see [Authors & Referees](#).

► Experimental design

Please check: are the following details reported in the manuscript?

1. Dimensions

Area of the tested solar cells

<input checked="" type="checkbox"/> Yes	Methods in the manuscript
<input type="checkbox"/> No	

Method used to determine the device area

<input checked="" type="checkbox"/> Yes	Methods in the manuscript
<input type="checkbox"/> No	

2. Current-voltage characterization

Current density-voltage (J-V) plots in both forward and backward direction

<input checked="" type="checkbox"/> Yes	Fig. 3b
<input type="checkbox"/> No	

Voltage scan conditions

For instance: scan direction, speed, dwell times

<input checked="" type="checkbox"/> Yes	Methods in main text
<input type="checkbox"/> No	

Test environment

For instance: characterization temperature, in air or in glove box

<input checked="" type="checkbox"/> Yes	Methods in main text
<input type="checkbox"/> No	

Protocol for preconditioning of the device before its characterization

<input checked="" type="checkbox"/> Yes	Methods in main text
<input type="checkbox"/> No	

Stability of the J-V characteristic

Verified with time evolution of the maximum power point or with the photocurrent at maximum power point; see ref. 7 for details.

<input checked="" type="checkbox"/> Yes	Supplementary Fig. 17, Newport certificated results
<input type="checkbox"/> No	

3. Hysteresis or any other unusual behaviour

Description of the unusual behaviour observed during the characterization

<input type="checkbox"/> Yes	Not relevant
<input checked="" type="checkbox"/> No	

Related experimental data

<input type="checkbox"/> Yes	Not relevant
<input checked="" type="checkbox"/> No	

4. Efficiency

External quantum efficiency (EQE) or incident photons to current efficiency (IPCE)

<input checked="" type="checkbox"/> Yes	Fig. 3d
<input type="checkbox"/> No	

A comparison between the integrated response under the standard reference spectrum and the response measure under the simulator

<input checked="" type="checkbox"/> Yes	In the main text
<input type="checkbox"/> No	

For tandem solar cells, the bias illumination and bias voltage used for each subcell

<input type="checkbox"/> Yes	<i>State where this information can be found in the text.</i>
<input type="checkbox"/> No	<i>Explain why this information is not reported/not relevant.</i>

5. Calibration

Light source and reference cell or sensor used for the characterization

<input checked="" type="checkbox"/> Yes	Methods in the main text
<input type="checkbox"/> No	

Confirmation that the reference cell was calibrated and certified

<input checked="" type="checkbox"/> Yes	Methods in the main text
<input type="checkbox"/> No	

Calculation of spectral mismatch between the reference cell and the devices under test	<input checked="" type="checkbox"/> Yes <input type="checkbox"/> No	It has been calibrated
6. Mask/aperture		
Size of the mask/aperture used during testing	<input checked="" type="checkbox"/> Yes <input type="checkbox"/> No	Methods in the main text
Variation of the measured short-circuit current density with the mask/aperture area	<input checked="" type="checkbox"/> Yes <input type="checkbox"/> No	Newport certification report in supplementary Fig. 17
7. Performance certification		
Identity of the independent certification laboratory that confirmed the photovoltaic performance	<input checked="" type="checkbox"/> Yes <input type="checkbox"/> No	Newport
A copy of any certificate(s) <i>Provide in Supplementary Information</i>	<input checked="" type="checkbox"/> Yes <input type="checkbox"/> No	Supplementary Fig. 17 and Fig. 18
8. Statistics		
Number of solar cells tested	<input checked="" type="checkbox"/> Yes <input type="checkbox"/> No	Supplementary Fig. 16
Statistical analysis of the device performance	<input checked="" type="checkbox"/> Yes <input type="checkbox"/> No	Supplementary Fig. 16
9. Long-term stability analysis		
Type of analysis, bias conditions and environmental conditions <i>For instance: illumination type, temperature, atmosphere humidity, encapsulation method, preconditioning temperature</i>	<input checked="" type="checkbox"/> Yes <input type="checkbox"/> No	Fig. 5 and Supplementary Fig. 24

Surface passivation of perovskite film for efficient solar cells

Qi Jiang^{1,2}, Yang Zhao^{1,2}, Xingwang Zhang^{1,2}, Xiaolei Yang¹, Yong Chen^{1,2}, Zema Chu^{1,2}, Qiufeng Ye^{1,2}, Xingxing Li^{1,2}, Zhigang Yin^{1,2} and Jingbi You^{1,2*}

In recent years, the power conversion efficiency of perovskite solar cells has increased to reach over 20%. Finding an effective means of defect passivation is thought to be a promising route for bringing further increases in the power conversion efficiency and the open-circuit voltage (V_{OC}) of perovskite solar cells. Here, we report the use of an organic halide salt phenethylammonium iodide (PEAI) on $\text{HC}(\text{NH}_2)_2\text{-CH}_3\text{NH}_3$ mixed perovskite films for surface defect passivation. We find that PEAI can form on the perovskite surface and results in higher-efficiency cells by reducing the defects and suppressing non-radiative recombination. As a result, planar perovskite solar cells with a certificated efficiency of 23.32% (quasi-steady state) are obtained. In addition, a V_{OC} as high as 1.18 V is achieved at the absorption threshold of 1.53 eV, which is 94.4% of the Shockley–Queisser limit V_{OC} (1.25 V).

The power conversion efficiency (PCE) of perovskite solar cells (PSCs) swiftly increased from 3.8% to more than 20% in 10 years due to composition engineering, perovskite film growth control and perovskite/transport layer interface engineering^{1–13}. To further increase the PCE of PSCs, improvement of the open-circuit voltage (V_{OC}) and fill factor (FF) could be more feasible than the short-circuit current (J_{SC}), considering that the J_{SC} is almost close to its limit (~26 mA cm⁻²) for a bandgap of around 1.55 eV.

It is known that the V_{OC} of solar cells is strongly related to the recombination of defects in the bulk or on the surface of the absorber layer^{14–17}. Solution-processed perovskite films are usually polycrystalline, which means they contain substantial structural disorder, such as grain boundary defects and crystallographic defects^{14–17}. Although it has been theoretically predicted that most of the defects formed in the perovskite layer are shallow defects¹⁸, several experimental results have shown that the suppression of defects in solution-processed perovskite films is critical for further enhancing the performance of PSCs towards their thermodynamic limits^{9,19,20}.

The surface is the place where defects are most easily formed, and passivation of the surface defects is always the most important task in any type of solar cells^{11,15,21}. In PSCs, several efficient surface passivation methods have been adopted. For example, excess PbI_2 in the perovskite layer, on the surface or at the grain boundary can suppress charge recombination by formation of I-type band alignment^{22–24}. Wide bandgap perovskites such as $\text{FAPbI}_{3-x}\text{Br}_x$ (ref. ²⁵), two-dimensional (2D) perovskite materials, for example, PEA_2PbI_4 and BA_2PbI_4 (refs. ^{26–31}), and super-thin insulated materials such as polystyrene¹⁵ have been utilized. More recently, several halide compounds such as quaternary ammonium halides¹¹, diammonium iodide²⁰, potassium halide³² and iodopentafluorobenzene³³ have been employed to passivate dangling bonds in the perovskite layer by exploiting the associated intermolecular interaction.

Here, we develop an organic halide salt, phenethylammonium iodide (PEAI), for post-treatment of mixed perovskites $\text{FA}_{1-x}\text{MA}_x\text{PbI}_3$ (FA : $\text{HC}(\text{NH}_2)_2$; MA : CH_3NH_3) to suppress the surface defects of perovskite polycrystalline films for efficient solar cells. Surprisingly, the organic halide salt PEAI, rather than the 2D

layered PEA_2PbI_4 perovskite proposed in many recent studies^{26–31}, serves as a much more effective passivation additive for a 3D perovskite. We carefully control the conversion process of PEAI to PEA_2PbI_4 in the actual devices using direct X-ray diffraction (XRD) evidence and show that the existence of PEAI instead of PEA_2PbI_4 in the perovskite thin-film devices is the key to increasing the V_{OC} to as high as 1.18 V, which is 94.4% of the Shockley–Queisser limit V_{OC} (1.25 V). As a result, a 23.32% certificated PSC has been achieved.

Design and fabrication of the perovskite films

The perovskite layer $\text{FA}_{1-x}\text{MA}_x\text{PbI}_3$ was deposited using a two-step spin-coating method^{18,24,34,35}, and the mixed organic salts FAI and MAI were diffused into the PbI_2 bottom layer via annealing. Comparing with previous reports and ours^{5,8,24}, we replaced the methylammonium bromide (MABr) in the traditional high-performance perovskite material $(\text{FAPbI}_3)_{1-x}(\text{MAPbBr}_3)_x$ with methylammonium iodine (MAI) to form $\text{FA}_{1-x}\text{MA}_x\text{PbI}_3$ perovskites, which is expected to further lower the absorption threshold of the perovskites to absorb more sunlight (Supplementary Fig. 1). We found that a small amount of MAI incorporation (8% in precursor) can stabilize the α -phase of FAPbI_3 (Fig. 1c), which is consistent with the tolerance factor empirical rule^{36,37}. To introduce a passivation layer, a PEAI salt solution was spin-coated onto the perovskite surface. It is noted that no additional process was carried out for PEAI layer. The device structure of the perovskite solar cells we adopted in this study is shown in Fig. 1a. We infer that the PEAI coating on the perovskite layer fills the iodine vacancies on the surface (Fig. 1b), and at the grain boundary (Supplementary Fig. 2), resulting in passivation of the surface defects and enhancement of the device performance²⁰.

Characterization of the perovskite films

We carried out grazing incident X-ray diffraction (GIXRD) for the perovskite films with and without a PEAI layer (Fig. 1c) to clearly show the states of PEAI on the surface. We found that the diffraction peaks for the perovskite with PEAI treatment are almost the same as for the control film without PEAI. However, a new diffraction

¹Key Laboratory of Semiconductor Materials Science, Institute of Semiconductors, Chinese Academy of Sciences, Beijing, China. ²Center of Materials Science and Optoelectronics Engineering, University of Chinese Academy of Sciences, Beijing, China. *e-mail: jyou@semi.ac.cn

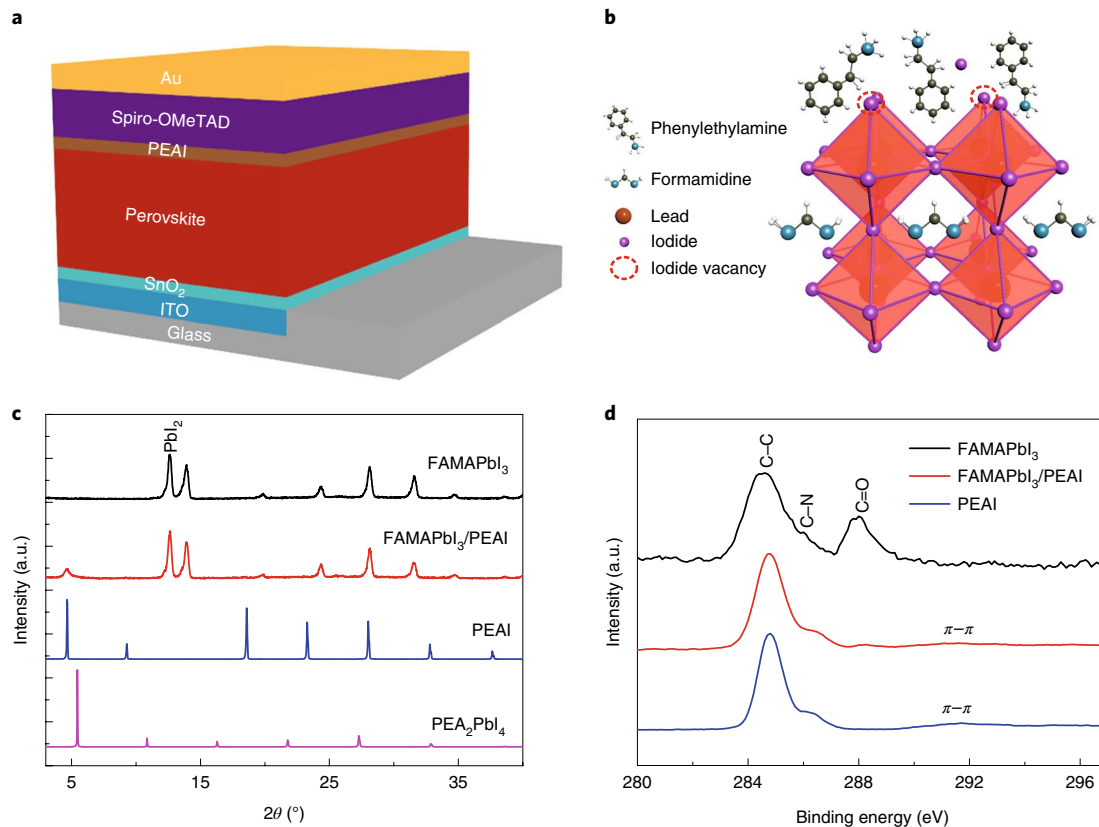


Fig. 1 | Device structure, possible passivation mechanism and states of PEAI on the perovskite surface. **a**, The device structure adopted in this study. PEAI is used for post-treatment of the perovskite surface. **b**, Possible passivation mechanism of the PEAI layer for the perovskite film. **c**, GIXRD patterns of perovskite films before and after PEAI treatment. The diffraction patterns of the PEAI powder and of the PEA_2PbI_4 film are also shown. **d**, XPS spectra of the perovskite before and after PEAI treatment, and of the pure PEAI film. The C 1s core-level energy spectra are shown for comparison.

peak appeared at 4.7° , which is consistent with the diffraction pattern for PEAI powder, and there is no obvious diffraction peak at 5.4° corresponding to the 2D perovskite PEA_2PbI_4 (Fig. 1c and Supplementary Fig. 3). It can be concluded that the dominant form of PEAI salt on the perovskite surface is the PEAI crystal itself, which is in contrast to previous reports on the formation of a 2D perovskite on a 3D perovskite surface^{26–31}. We will show that PEAI itself has a much better passivation effect than a 2D PEA_2PbI_4 thin layer. From scanning electron microscopy results (Supplementary Fig. 2a,b), we found that the perovskite surface was covered by a PEAI layer. In addition, the roughness of the perovskite layer was reduced from 32 to 24 nm according to atomic force microscopy results (Supplementary Fig. 2c,d), indicating that the PEAI salt is more easily deposited at the grain boundary (usually, the grain boundary is the deepest place on the surface, Supplementary Fig. 7). Therefore, this reduces the height difference between the grain surface and the grain boundary.

We conducted X-ray photoelectron spectroscopy (XPS) measurements to confirm the existence of PEAI on perovskite (Fig. 1d). For the perovskite with PEAI treatment, in addition to C–C and C–N peaks located at 284.6 eV and 286.1 eV, respectively, we also found that a peak emerges at a binding energy of 292.0 eV, consistent with $\pi-\pi$ bonding in the phenyl functional group of the PEA^+ cations²⁶. We also noticed that the C=O peak (288.1 eV) seen for the control film associated with oxygen/moisture is significantly suppressed after PEAI modification, indicating that the PEAI coating can slow the degradation of the perovskite layer. Furthermore, according to the Pb 4f and I 3d core-level energy spectra (Supplementary Fig. 4), it can be estimated that the Pb:I ratio for the control perovskite film

is 1:1.55, which indicates that the surface is seriously iodine deficit, which could lead to obvious point defects (Fig. 1b). After PEAI modification, the Pb:I ratio dramatically increased to 1:2.34, indicating the presence of abundant iodide on the perovskite surface and that the iodine vacancy is likely to be filled (Fig. 1b).

We monitored the steady photoluminescence (PL) of the perovskite films with PEAI treatment under different conditions (Fig. 2a). We found that the PL intensities are obviously increased after PEAI treatment without additional thermal annealing, indicating that recombination in the perovskite layer has been largely suppressed^{38,39}. We also mapped the PL intensities of perovskite films with 470 nm excitation (Supplementary Fig. 5), and found that the PL from the perovskite films with PEAI treatment becomes much more intense and uniform compared with the control film. Owing to the strong absorption of perovskite at short wavelengths, we anticipate that only the perovskite surface (<100 nm) is excited when using 470 nm excitation. Therefore, strong PL enhancement indicates that PEAI treatment suppresses the surface non-radiative recombination defects. According to the time-resolved PL results (Fig. 2b, Supplementary Fig. 6 and Supplementary Table 1), the carrier lifetime of the perovskite is significantly increased from 0.3 μ s to more than 2 μ s, and the recombination rate has been reduced by fivefold after PEAI treatment.

It is interesting that we found that the PL intensity and lifetime of the perovskite films become slightly weaker and shorter when the PEAI layer is annealed above 50 °C (Fig. 2a,b). This phenomenon becomes more obvious for thermal annealing of the perovskite/PEAI film at 100 °C (Fig. 2a,b), and the PEAI-treated perovskite film shows almost the same emission properties as the control film,

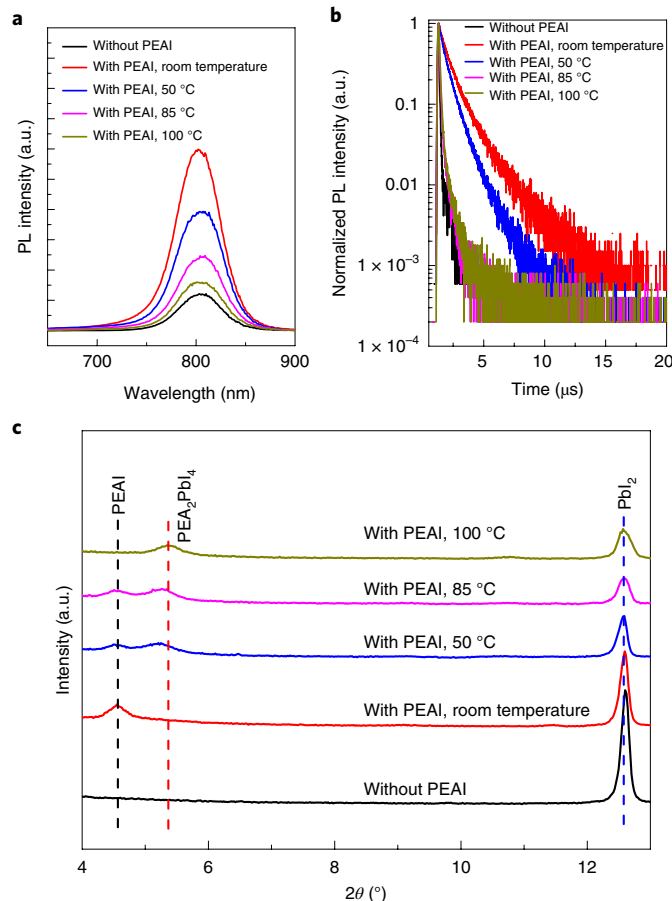


Fig. 2 | Surface passivation of perovskite layer by PEAI. **a**, Steady PL of the perovskite films with PEAI treatment under different conditions. **b**, Time-resolved PL of the perovskite films with PEAI treatment under different conditions. **c**, XRD of perovskite films with PEAI treatment under different conditions.

indicating that the passivation effect has almost disappeared. From the XRD results (Fig. 2c), we found that the PEAI is gradually converted into the PEA_2PbI_4 phase during the thermal annealing process, and when the perovskite/PEAI layer is annealed at 100 °C for 5 min, the PEAI crystal diffraction totally disappears (Fig. 2c). According to the PL and XRD results (Fig. 2), it can be concluded that the PEAI itself shows a much better passivation effect than the 2D perovskite of PEA_2PbI_4 . Therefore, in this study, we utilized the PEAI layer, not the conventional 2D perovskite^{26–31}, to passivate the defects in the perovskite layer.

Device fabrication and characterization

Keeping in mind that PEAI can efficiently passivate the surface defects in the perovskite layer, we fabricated devices with the structure ITO/SnO₂/perovskite/spiro-OMeTAD/Au^{8,24} (ITO: indium tin oxide; spiro-OMeTAD: 2,2',7,7'-tetrakis(*N,N*-dimethoxyphenylamine)-9,9'-spirobifluorene). The thicknesses of the electron transport layer SnO₂, the perovskite layer and the hole transport layer spiro-OMeTAD were about 40 nm, 800 nm and 250 nm, respectively (Supplementary Fig. 7). The dependence of the device performance on the PEAI concentration (Fig. 3a, Supplementary Fig. 8 and Supplementary Table 2) shows that the PCE jumped significantly when the perovskite films were treated with a low concentration of PEAI solution, and the PCE reached a maximum at 20 mM of PEAI. For this best condition, the mass

thickness of the PEAI is about 16 nm when deposited on a smooth silicon substrate (Supplementary Fig. 9). It is noted that several tens of nanometres of PEAI films deposited on a very rough perovskite surface (roughness = 32 nm, Supplementary Fig. 2) via a solution process cannot be conformal, and the resulting PEAI film should be discontinuous or thin enough for charge transport (Supplementary Fig. 10). While the device performance began to drop at high PEAI loading even the recombination rate was low (Supplementary Fig. 6), which could be due to the highly insulating properties of PEAI. The typical *J–V* curve of the device with PEAI (20 mM) and without PEAI treatment is shown in Fig. 3b. It can be seen that the J_{SC} remains almost the same, while V_{OC} substantially increases compared with the control device. We also observed that the hysteresis can be eliminated when the perovskite surface is treated with PEAI. Both the improvement of device performance and elimination of hysteresis could be related to the reduction of the surface defects, which can result in suppression of charge recombination and also charge accumulation²⁰.

We tested the device performance when the PEAI layer was processed at different temperatures and found that the device performance degraded while thermal annealing the PEAI layer (Supplementary Fig. 11 and Supplementary Table 3). This is consistent with the PL results (Fig. 2a,b), confirming that the PEAI itself has a better passivation effect for perovskite layer. We also screened several organic iodine salts for perovskite surface treatment and found that the device performance either showed no significant enhancement or inferior performance compared with the control device (Supplementary Fig. 12 and Supplementary Table 4).

After optimization of the PEAI-treated device, we obtained the best device with an efficiency of 23.56%, a V_{OC} as high as 1.16 V, a J_{SC} of 24.9 mA cm^{−2} and a fill factor (FF) of 81.4% (Fig. 3c), and there is almost no hysteresis for the device (Supplementary Fig. 13 and Supplementary Table 5). The steady output for the best device shows a quasi-steady output of 23.2%, while for the device without PEAI, the output is 21.3% (Supplementary Fig. 14). The integrated current density from the external quantum efficiency (EQE) is 24.5 mA cm^{−2} (Fig. 3d), which is almost in agreement with the measurement from the solar simulator in this study. In addition, according to the EQE decrease to half the peak value and the differential of the EQE⁴⁰, it can be estimated that the absorption threshold is 1.53 eV. This value is consistent with the result from the differential of absorption (Supplementary Fig. 15). The statistics of the PCE distribution confirm the reproducibility of our results and that the PEAI treatment can undoubtedly improve the performance of PSCs (Supplementary Fig. 16).

We sent the best device to an accredited laboratory (Newport, USA) for certification. The devices showed 23.32% certified efficiency with a V_{OC} of 1.18 V, J_{SC} of 25.2 mA cm^{−2} and FF of 78.4% (Supplementary Figs. 17 and 18). Furthermore, it is noted that the certified efficiency obtained here is the quasi-steady-state efficiency⁴¹. In this new measurement standard, the *J–V* parameters were measured under a 13-point IV sweep configuration wherein the bias voltage (current for V_{OC} determination) is held constant until the measured current (voltage for V_{OC}) is determined to be unchanging at the 0.03% level. This is intended to represent the quasi-steady-state performance of the device.

We tested the device response under different light intensities (Supplementary Fig. 19). We found that both the control and PEAI-treated devices show a linear J_{SC} versus light intensity relationship (Supplementary Fig. 19c). This indicates that carriers can transport smoothly in the device and that there is no obvious charge barrier induced at the interface even though insulating PEAI was introduced. The relationship between V_{OC} and light intensity is also plotted (Fig. 4a). It can be seen that the control device shows a slope of $1.88k_{\text{B}}T/q$, while PEAI-treated devices show a much smaller slope

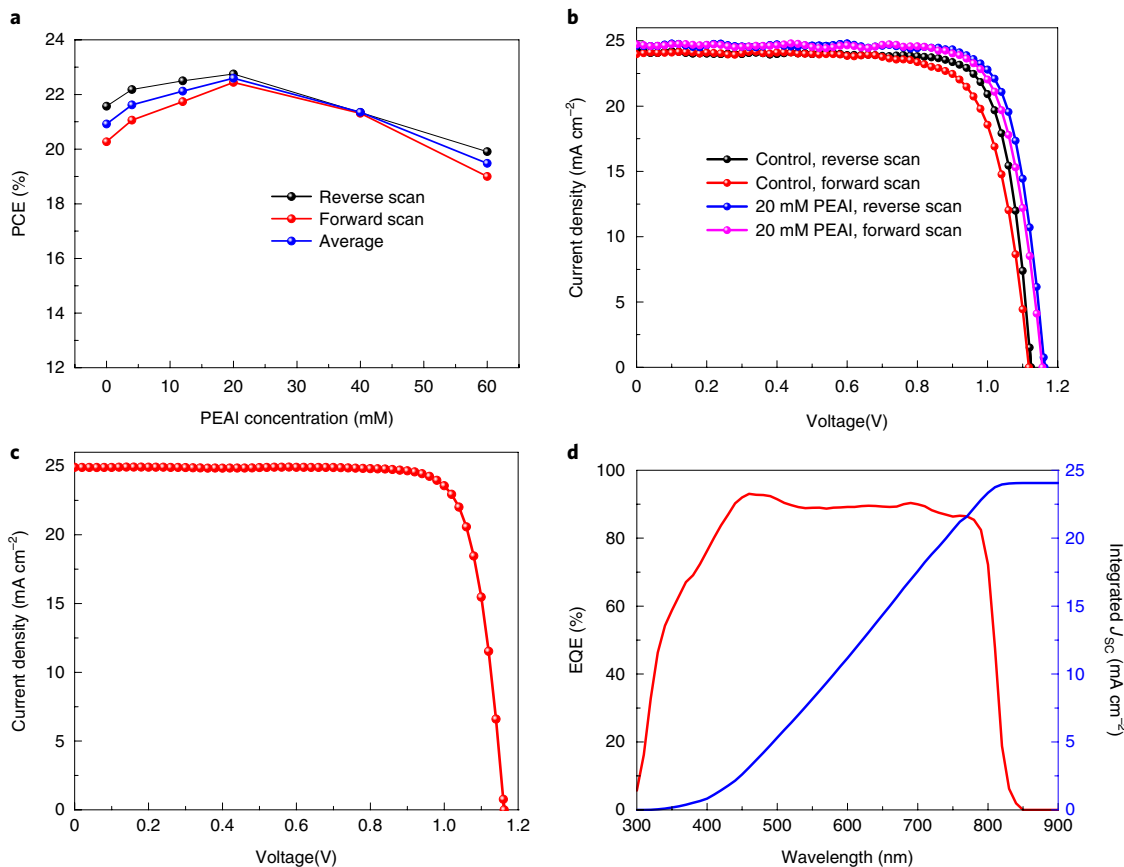


Fig. 3 | Device performance. **a**, The dependence of device performance on concentration of PEAI solution. Reverse scan (1.2 V to 0 V) and forward scan (0 V to 1.2 V) were both collected, and the average of the reverse and forward scans is included. **b**, The typical J - V curve of the device with PEAI (20 mM) and without PEAI treatment under one-sun (100 mW cm^{-2}) conditions. The reverse and forward scans are both included. **c**, The best device we achieved in our laboratory by optimizing the PEAI condition (20 mM). A 23.56% PCE is achieved with a V_{oc} of 1.16 V, J_{sc} of 24.9 mA cm^{-2} and FF of 81.4%. **d**, EQE of the best device. The integrated J_{sc} from the EQE is 24.5 mA cm^{-2} .

($1.27k_B T/q$), where k_B is the Boltzmann constant, T is temperature and q is the electric charge. It is known that deviation of the slope from $k_B T/q$ reflects defect-assisted recombination in the devices⁴². These results further confirmed that the recombination has largely been suppressed in the perovskite layer.

We derived the charge recombination and transport time constants (τ_r and τ_t , respectively) from the transient photovoltage and photocurrent decays measured at open and short circuit, respectively⁴³. The τ_r of the PEAI-treated device is as high as $138.2 \mu\text{s}$ (Fig. 4b), which is even longer than that of MAPbI₃ perovskite single-crystal devices under one-sun conditions⁴⁴. Furthermore, this value is substantially longer than that of the control device (versus $8.8 \mu\text{s}$, Fig. 4b), which could be attributed to slower surface charge recombination. We also found that the τ_t slightly decreases from $3 \mu\text{s}$ to $2.3 \mu\text{s}$ after PEAI treatment (Supplementary Fig. 20). The insertion of insulting PEAI cannot enhance the hole extraction from perovskite to spiro-OMeTAD and decrease τ_t . Therefore, the slight reduction of τ_t could also be due to the reduction of charge recombination on introduction of PEAI.

A V_{oc} as high as 1.18 V is obtained (Supplementary Figs. 17 and 18), which is 94.4% of the Shockley–Queisser limit V_{oc} (1.25 V) for the absorption threshold of 1.53 eV (ref. ⁴⁵). In addition, there is only 0.35 V of V_{oc} loss ($E_{abs}/q - V_{oc}$) at the absorption threshold (E_{abs}) 1.53 eV, which is even less than that of crystal silicon solar cells (0.38 V) and comparable to GaAs solar cells (0.30 V)¹³. It has been shown that the EQE of the EL of the solar cells under bias voltage (operating as a light-emitting diode (LED)) can be used to estimate

the recombination in the devices⁴⁵. Higher radiative recombination emission efficiency could deliver high V_{oc} based on the equation:

$$V_{oc} = \frac{k_B T}{q} \ln \left(\text{EQE}_{EL} \frac{J_{ph}}{J_{em,0}} + 1 \right) \quad (1)$$

where EQE_{EL} is quantum efficiency when the injection current in the dark is equal to the photocurrent (J_{ph}) of the device under light illumination and $J_{em,0}$ is the current of re-emitted photons at room temperature⁴⁵.

We tested the solar cell device operating as a LED in the dark and under a voltage bias. We found that PEAI-treated devices showed obvious EL and an emission peak located at 805 nm (Fig. 4c). Furthermore, the device can even emit under lower applied voltage (1.2 V), which is lower than the absorption threshold of perovskite (1.53 eV)—the apparent violation of energy conservation could come from heat extracted from the diode⁴⁶. It is encouraging that the device showed close to 7% EL efficiency under an injection current of 25.2 mA cm^{-2} (equal to short-circuit current $J_{sc} = J_{ph}$) (Fig. 4d and Supplementary Fig. 21). For comparison, the control device only shows 0.8% EL efficiency under same injection current (Fig. 4d and Supplementary Fig. 21). Based on equation (1), it can be estimated that the V_{oc} improvement (ΔV_{oc}) after PEAI treatment is: $\Delta V_{oc} = k_B T/q \ln(\text{EQE}_{PEAI}/\text{EQE}_{without PEAI}) = 0.056 \text{ V}$. This result is almost consistent with the J - V results, while the control and PEAI-treated devices showed V_{oc} around 1.12 V and 1.18 V, respectively.

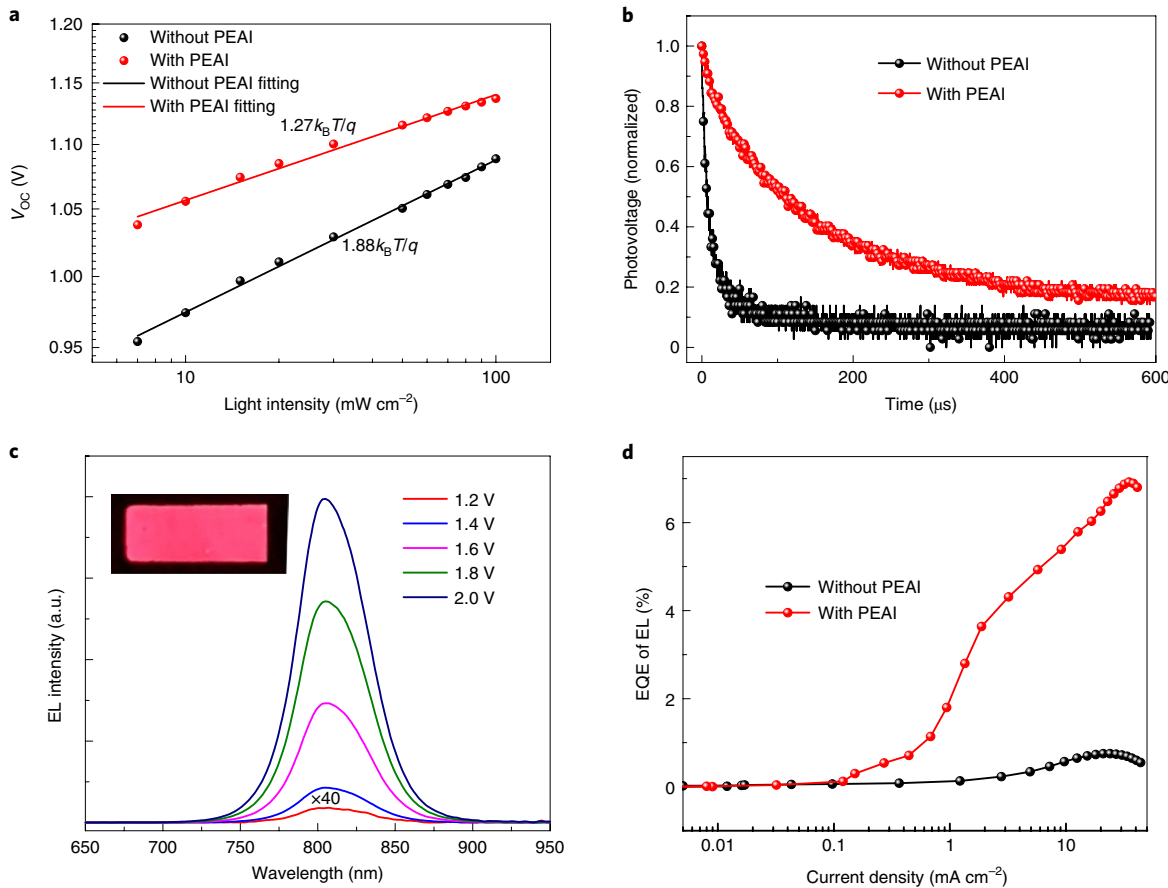


Fig. 4 | Characterization of the devices. **a**, V_{oc} versus light intensity for the PSCs with and without PEAI. **b**, Normalized transient photovoltage decay curves for the solar cells with and without PEAI. **c**, EL spectra of the devices with PEAI under different voltage bias operating as LEDs. Inset: EL image of the devices under different voltage bias. **d**, EQE of EL of the devices while operating as LEDs.

We also calculated the internal quantum efficiency of the devices, which were 9.7% and 50.4% for the control and PEAI-treated devices, respectively, according to the relationship between external and internal emission^{47,48}. This result shows that the non-radiative losses in the perovskite layer have been significantly suppressed by PEAI passivation. We could increase the V_{oc} close to its limit (1.25 V) if we could fully suppress the non-radiative recombination in the perovskite layer, on the surface or at the interface, and then the PCE of PSCs could be improved beyond 25%.

Stability of the devices

We tested the device stability at 85 °C for more than 500 h (Fig. 5). A more thermally stable hole transport layer poly[bis(4-phenyl)(2,4,6-trimethylphenyl)amine] (PTAA) was used to replace spiro-OMeTAD for thermal stability testing^{49,50}. The initial PCE of the PEAI-treated devices with a PTAA hole transport layer was 19.1% (Supplementary Fig. 22 and Supplementary Table 6), which is lower than the best device performance using spiro-OMeTAD as the hole transport layer. This is a common issue and could be addressed in future studies. We found that the PCE of the PEAI-treated device decreased at the start of several hours of annealing at 85 °C, and then the performance remained almost constant up to 500 h of heating. Time-resolved PL for the perovskite films/hole transport layer showed that the lifetime of the perovskite layer was significantly shortened in minutes after heating at 85 °C (Supplementary Fig. 23). This is fully consistent with the results shown in Fig. 2b. Then there is no obvious change when the heating time is extended to hours (Supplementary Fig. 23). The shortening of lifetime during

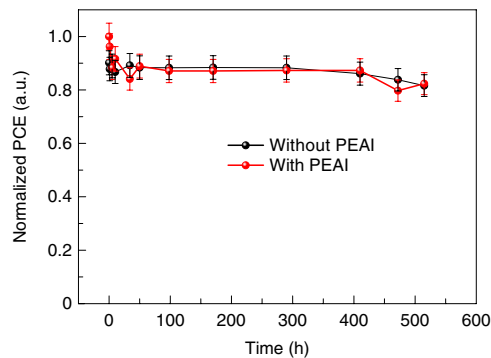


Fig. 5 | Thermal stability of the devices. The thermal stability (85 °C) of the devices with and without PEAI layers. Up to 500 h stability was tested. PTAA was used to replace spiro-OMeTAD as the hole transport layer for thermal testing. The device performance without PEAI has been divided by the initial device performance of PEAI-based devices, and the initial performance of the devices with PEAI has been normalized. The starting efficiency of the cells is 19.1% and 17.2% for the devices with and without a PEAI layer, respectively (Supplementary Fig. 22 and Supplementary Table 6). For each type of device, ten devices were utilized for the thermal stability test, 5% of error bars has been adopted.

heating could be ascribed to the disappearance of the passivation effect by converting PEAI into PEA_2PbI_4 according to Fig. 2, which results in device performance degradation during heating.

These results showed that the thermal stability of PEAI-based devices is not good enough, and that other passivation materials with good thermal stability should be screened. We also preliminarily tested the device stability under continuous light soaking at the maximum power point (25°C , 100 mW cm^{-2}) and found that there is no obvious decrease in device performance over 40 h (Supplementary Fig. 24).

In summary, we have provided an efficient and simple method for passivation of the perovskite surface through which the defects are significantly reduced and the recombination is suppressed. As a result, a 23.32% certificated efficiency was obtained by adopting a low-temperature solution-processed planar structure. This method could be helpful for obtaining low-cost, efficient and highly flexible solar cells.

Online content

Any methods, additional references, Nature Research reporting summaries, source data, statements of data availability and associated accession codes are available at <https://doi.org/10.1038/s41566-019-0398-2>.

Received: 28 August 2018; Accepted: 25 February 2019;

Published online: 1 April 2019

References

- Kojima, A., Teshima, K., Shirai, Y. & Miyasaka, T. Organometal halide perovskites as visible-light sensitizers for photovoltaic cells. *J. Am. Chem. Soc.* **131**, 6050–6051 (2009).
- Kim, H. S. et al. Lead iodide perovskite sensitized all-solid-state submicron thin film mesoscopic solar cell with efficiency exceeding 9%. *Sci. Rep.* **2**, 591 (2012).
- Lee, M. M., Teuscher, J., Miyasaka, T., Murakami, T. N. & Snaith, H. J. Efficient hybrid solar cells based on meso-superstructured organometal halide perovskites. *Science* **338**, 643–647 (2012).
- Zhou, H. et al. Interface engineering of highly efficient perovskite solar cells. *Science* **345**, 542–546 (2014).
- Jeon, N. J. et al. Compositional engineering of perovskite materials for high-performance solar cells. *Nature* **517**, 476–480 (2015).
- Nie, W. et al. High efficiency millimeter-scale crystalline perovskite solar cells. *Science* **347**, 522–525 (2015).
- Bi, D. et al. Polymer-templated nucleation and crystal growth of perovskite films for solar cells with efficiency greater than 21%. *Nat. Energy* **1**, 16142 (2016).
- Jiang, Q. et al. Enhanced electron extraction using SnO_2 for high-efficiency planar-structure $\text{HC}(\text{NH}_2)_2\text{PbI}_3$ -based perovskite solar cells. *Nat. Energy* **2**, 16177 (2016).
- Tan, H. et al. Efficient and stable solution-processed planar perovskite solar cells via contact passivation. *Science* **355**, 722–726 (2017).
- Anaraki, E. H. et al. Highly efficient and stable planar perovskite solar cells by solution-processed tin oxide. *Energy Environ. Sci.* **9**, 3128–3134 (2016).
- Zheng, X. et al. Defect passivation in hybrid perovskite solar cells using quaternary ammonium halide anions and cations. *Nat. Energy* **2**, 17102 (2017).
- Yang, W. S. et al. Iodide management in formamidinium-lead-halide-based perovskite layers for efficient solar cells. *Science* **356**, 1376–1379 (2017).
- Green, M. A. et al. Solar cell efficiency tables (version 51). *Prog. Photovolt. Res. Appl.* **26**, 3–12 (2018).
- Wetzelra, G. A. H. et al. Trap-assisted non-radiative recombination in organic-inorganic perovskite solar cells. *Adv. Mater.* **27**, 1837–1841 (2015).
- Wang, Q. et al. Thin insulating tunneling contacts for efficient and water-resistant perovskite solar cells. *Adv. Mater.* **28**, 6734–6739 (2016).
- Manser, J. S., Saidaminov, M. I., Christians, J. A., Bakr, O. M. & Kamat, P. V. Making and breaking of lead halide perovskites. *Acc. Chem. Res.* **49**, 330–338 (2016).
- Buin, A. et al. Materials processing routes to trap-free halide perovskites. *Nano Lett.* **14**, 6281–6286 (2014).
- Yin, W. J., Shi, T. & Yan, Y. Unusual defect physics in $\text{CH}_3\text{NH}_3\text{PbI}_3$ perovskite solar cell absorber. *Appl. Phys. Lett.* **104**, 063903 (2014).
- de Quilettes, D. W. et al. Impact of microstructure on local carrier lifetime in perovskite solar cells. *Science* **348**, 683–686 (2015).
- Zhao, T., Chueh, C. C., Chen, Q., Rajagopal, A. & Jen, A. K. Y. Defect passivation of organic-inorganic hybrid perovskites by diammonium iodide toward high-performance photovoltaic devices. *ACS Energy Lett.* **1**, 757–763 (2016).
- Yoshikawa, K. et al. Silicon heterojunction solar cell with interdigitated back contacts for a photoconversion efficiency over 26%. *Nat. Energy* **2**, 17032 (2017).
- Chen, Q. et al. Controllable self-induced passivation of hybrid lead iodide perovskites toward high performance solar cells. *Nano Lett.* **14**, 4158–4163 (2014).
- Wang, L., McCleese, C., Kovalsky, A., Zhao, Y. & Burda, C. Femtosecond time-resolved transient absorption spectroscopy of $\text{CH}_3\text{NH}_3\text{PbI}_3$ perovskite films: evidence for passivation effect of PbI_2 . *J. Am. Chem. Soc.* **136**, 12205–12208 (2014).
- Jiang, Q. et al. Planar-structure perovskite solar cells with efficiency beyond 21%. *Adv. Mater.* **29**, 1703852 (2017).
- Cho, K. T. et al. Highly efficient perovskite solar cells with a compositionally engineered perovskite/hole transporting material interface. *Energy Environ. Sci.* **10**, 621–627 (2017).
- Chen, P. et al. In situ growth of 2D perovskite capping layer for stable and efficient perovskite solar cells. *Adv. Funct. Mater.* **28**, 1706923 (2018).
- Cho, K. T. et al. Selective growth of layered perovskites for stable and efficient photovoltaics. *Energy Environ. Sci.* **11**, 952–959 (2018).
- Lin, Y. et al. Enhanced thermal stability in perovskite solar cells by assembling 2D/3D stacking structures. *J. Phys. Chem. Lett.* **9**, 654–658 (2018).
- Yoo, H. S. & Park, N. G. Post-treatment of perovskite film with phenylalkylammonium iodide for hysteresis-less perovskite solar cells. *Sol. Energy Mater. Sol. Cells* **179**, 57–65 (2018).
- Li, N. et al. Enhanced moisture stability of cesium-containing compositional perovskites by a feasible interfacial engineering. *Adv. Mater. Interfaces* **4**, 1700598 (2017).
- Abdi-Jalebi, M. et al. Maximizing and stabilizing luminescence from halide perovskites with potassium passivation. *Nature* **555**, 497–501 (2018).
- Abate, A. et al. Supramolecular halogen bond passivation of organic-inorganic halide perovskite solar cells. *Nano Lett.* **14**, 3247–3254 (2014).
- Xiao, Z. et al. Efficient, high yield perovskite photovoltaic devices grown by interdiffusion of solution-processed precursor stacking layers. *Energy Environ. Sci.* **7**, 2619–2623 (2014).
- Im, J. H., Jang, I. H., Pellet, N., Gratzel, M. & Park, N. G. Growth of $\text{CH}_3\text{NH}_3\text{PbI}_3$ cuboids with controlled size for high-efficiency perovskite solar cells. *Nat. Nanotechnol.* **9**, 927–932 (2014).
- Li, Z. et al. Stabilizing perovskite structures by tuning tolerance factor: formation of formamidinium and cesium lead iodide solid-state alloys. *Chem. Mater.* **28**, 284–292 (2016).
- Pellet, N. et al. Mixed-organic-cation perovskite photovoltaics for enhanced solar-light harvesting. *Angew. Chem. Int. Ed.* **53**, 3151–3157 (2014).
- Li, X. et al. A vacuum flash-assisted solution process for high-efficiency large-area perovskite solar cells. *Science* **353**, 58–62 (2016).
- Noel, N. K. et al. Enhanced photoluminescence and solar cell performance via Lewis base passivation of organic-inorganic lead halide perovskites. *ACS Nano* **8**, 9815–9821 (2014).
- Green, M. A., Jiang, Y., Soufiani, A. M. & Ho-Baillie, A. Optical properties of photovoltaic organic-inorganic lead halide perovskites. *J. Phys. Chem. Lett.* **6**, 4774–4785 (2015).
- Snaith, H. J. et al. Anomalous hysteresis in perovskite solar cells. *J. Phys. Chem. Lett.* **5**, 1511–1515 (2014).
- Yang, D. et al. Surface optimization to eliminate hysteresis for record efficiency planar perovskite solar cells. *Energy Environ. Sci.* **9**, 3071–3078 (2016).
- Chen, W. et al. Efficient and stable large-area perovskite solar cells with inorganic charge extraction layers. *Science* **350**, 944–948 (2015).
- Dong, Q. et al. Electron-hole diffusion lengths $>175\text{ }\mu\text{m}$ in solution-grown $\text{CH}_3\text{NH}_3\text{PbI}_3$ single crystals. *Science* **347**, 967–970 (2015).
- Tress, W. et al. Predicting the open-circuit voltage of $\text{CH}_3\text{NH}_3\text{PbI}_3$ perovskite solar cells using electroluminescence and photovoltaic quantum efficiency spectra: the role of radiative and non-radiative recombination. *Adv. Energy Mater.* **5**, 1400812 (2015).
- Dousmanis, G. C., Mueller, C. W., Nelson, H. & Petzinger, K. G. Evidence of refrigerating action by means of photon emission in semiconductor diodes. *Phy. Rev.* **133**, A316–A318 (1964).
- Braly, I. L. et al. Hybrid perovskite films approaching the radiative limit with over 90% photoluminescence quantum efficiency. *Nat. Photon.* **12**, 355–361 (2018).
- Qian, D. et al. Design rules for minimizing voltage losses in high-efficiency organic solar cells. *Nat. Mater.* **17**, 703–709 (2018).
- Saliba, M. et al. Incorporation of rubidium cations into perovskite solar cells improves photovoltaic performance. *Science* **354**, 206–209 (2016).
- Meng, L. et al. Tailored phase conversion under conjugated polymer enables thermally stable perovskite solar cells with efficiency exceeding 21%. *J. Am. Chem. Soc.* **140**, 17255–17262 (2018).

Acknowledgements

This work is supported by the National Natural Science Foundation of China (grant numbers 61634001 and 61574133), the National Key Research and Development Program of China (grant number 2016YFB0700700), the Beijing Municipal Science & Technology Commission (grant numbers Z181100004718005 and Z181100005118002) and also by the National 1000 Young Talents awards. We thank Y. S. Liu from Nankai University for helping with the transit photovoltaic and photocurrent characterizations, and C. Y. Zhou from Enlitech for helping with the photoluminescence mapping measurement.

Author contributions

J.Y. conceived the idea, directed and supervised the project. Q.J. initialized this project, fabricated and characterized the devices. Y.Z. took part in the device fabrication and characterizations. X.Z., X.Y., C.Y., Z.C., Q.Y., X.L. and Z.Y. were involved in the data

analysis. J.Y., J.Q., Y.Z. and X.Z. co-wrote the manuscript. All authors contributed to discussions and to finalizing the manuscript.

Competing interests

The authors declare no competing interests.

Additional information

Supplementary information is available for this paper at <https://doi.org/10.1038/s41566-019-0398-2>.

Reprints and permissions information is available at www.nature.com/reprints.

Correspondence and requests for materials should be addressed to J.Y.

Publisher's note: Springer Nature remains neutral with regard to jurisdictional claims in published maps and institutional affiliations.

© The Author(s), under exclusive licence to Springer Nature Limited 2019

Methods

Materials. SnO_2 colloid precursor (tin (iv) oxide, 15% in H_2O colloidal dispersion) was purchased from Alfa Aesar. Dimethylformamide (DMF), dimethyl sulfoxide (DMSO) and lead iodine (PbI_2) were purchased from Sigma Aldrich. Formamidinium iodide (FAI), methylammonium bromide (MABr), methylammonium iodide (MAI), methylammonium chloride (MACl) and phenethylammonium iodide (PEAI) were all purchased from Xi'an Polymer Light Technology in China.

Solar cell fabrication. ITO glass was cleaned by sequentially washing with detergent, deionized water, acetone and isopropanol (IPA). Before use, the ITO was cleaned with ultraviolet ozone for 10 min. Then the substrate was spin-coated with a thin layer of SnO_2 nanoparticle film (2.67%, diluted by water) at 4,000 r.p.m. for 30 s, and annealed in ambient air at 150 °C for 30 min. It is better to clean the substrate with ultraviolet ozone for 10 min to improve the surface wetting. After that, 1.5 M of PbI_2 in DMF:DMSO (9:1) solvent was spin-coated onto SnO_2 at 1,500 r.p.m. for 30 s, then annealed at 70 °C for 1 min, and then cooled to room temperature. For FAMAPbI₃ perovskite film deposition, a solution of FAI:MAI:MACl (90 mg:6.39 mg:9 mg in 1 ml IPA) was spin-coated onto the PbI_2 at spin rate of 2,000 r.p.m. for 30 s, followed by thermal annealing at 150 °C for 15 min in ambient air conditions (30–40% humidity). For comparison, a $(\text{FAPbI}_3)_{1-x}(\text{MAPbBr}_3)_x$ mixed perovskite were also synthesized. A solution of FAI:MABr:MACl (90 mg:9 mg:9 mg in 1 ml IPA) was spin-coated onto the PbI_2 at spin rate of 2,000 r.p.m. for 30 s, followed by thermal annealing at 150 °C for 15 min in ambient air conditions (30–40% humidity). After perovskite formation, the samples were transferred to a nitrogen-filled glove box for further processing. For PEAI treatment, the PEAI solution was dissolved in IPA with different concentrations ranging from 0 mM to 60 mM and spin-coated onto the perovskite surface at a spin rate of 5,000 r.p.m. without any further processing. Then the hole transporting layer was deposited on top of the perovskite layer at a spin rate of 3,000 r.p.m. for 30 s using spiro-OMeTAD solution, which consisted of 72.3 mg spiro-OMeTAD, 35 µl bis(trifluoromethane) sulfonimide lithium salt (LiTFSI) stock solution (260 mg LiTFSI in 1 ml acetonitrile), 30 µl 4-tertbutylpyridine and 1 ml chlorobenzene. For the device thermal stability test, PTAA doped with poly[bis(4-phenyl)(2,4,6-trimethylphenyl)amine] (TPFB) was used to replace spiro-OMeTAD as the hole transport layer. The concentration of PTAA was 30 mg ml⁻¹ and the weight ratio of PTAA/TPFB was 10:1 (ref. ⁵⁰). The PTAA was deposited on top of the perovskite layer at a spin rate of 2,000 r.p.m. for 30 s. Finally, 80 nm of Au film was thermally evaporated as a counter electrode using a shadow mask. The device size areas were 0.108 cm². When measuring, a 0.0739 cm² non-reflective mask was used to define the accurate active cell area.

Material and device characterization. The scanning electron microscopy images was acquired using a field-emission scanning electron microscopy (FEI NanoSEM650), which uses an electron beam accelerated at 500 V to 30 kV, enabling operation at a variety of currents. Atomic force microscopy measurements were carried out using a Solver P47 PRO. The XRD patterns of the perovskite thin films were obtained on a Rigaku D/MAX-2500 system using $\text{Cu K}\alpha$ radiation ($\lambda = 1.5405 \text{ \AA}$) as the X-ray source. Scans were taken with a 0.5-mm-wide source and detector slits, with X-ray generator settings at 40 kV and 30 mA. For conventional XRD, a $\theta-2\theta$ model was used. For the GIXRD measurement, the incident angle was 0.5°. Absorption spectra were obtained using an ultraviolet-visible spectrometer (Cary 5000). Steady-state PL was measured by a FLS980 spectrometer. Time-resolved PL spectra were obtained using a F900 spectrometer. XPS was performed on a Thermo Scientific ESCALab 250Xi using 200 W monochromated Al $\text{K}\alpha$ (1486.6 eV) radiation. A 500 µm X-ray spot was used for XPS analysis. The base pressure in the analysis chamber was about 3×10^{-10} mbar. For the PL mapping, a laser scanning confocal microscope (Enlitech, SPCM-1000) equipped with a 470 nm pulse laser and galvo-based scanner was used. The objective was $\times 50$ with numerical aperture of 0.8; for this objective, the confocal pinhole was set to 50 µm size. The detector was a photo-multiplier tube (Hamamatsu) with a photon-counting module. The laser source was set to 1 µW range on the sample for measurement. Transient photocurrent and photovoltaic measurements were measured on a home-made system similar to that previously reported⁸. For the device operating as a LED, the device was mounted in an integrating sphere and the power output measured for calculation of the EQE (Enlitech, LQE-50-PL). The $J-V$ characteristics of the photovoltaic cells were obtained using a Keithley 2400 Source Meter under simulated one-sun AM 1.5G illumination (100 mW cm⁻²) with a solar simulator (Enlitech, SS-F5-3A) and the light intensity was calibrated by means of a KG-5 Si diode. The $J-V$ measurements were carried out in ambient air. The devices were measured both in reverse scan (1.2 V → 0 V, step 0.02 V) and forward scan (0 V → 1.2 V, step 0.02 V). The EQE was measured using an Enlitech EQE measurement system (QE-R3018). We sent the best devices to an accredited laboratory (Newport, USA) for certification. The device thermal stability tests were carried out in a nitrogen glove box, and the devices were put on a hotplate with a temperature of 85 °C.

Reporting Summary. Further information on research design is available in the Nature Research Reporting Summary linked to this article.

Data availability

The data that support the plots within this paper and other findings of this study are available from the corresponding author upon reasonable request.

Solar Cells Reporting Summary

Nature Research wishes to improve the reproducibility of the work that we publish. This form is intended for publication with all accepted papers reporting the characterization of photovoltaic devices and provides structure for consistency and transparency in reporting. Some list items might not apply to an individual manuscript, but all fields must be completed for clarity.

For further information on Nature Research policies, including our [data availability policy](#), see [Authors & Referees](#).

► Experimental design

Please check: are the following details reported in the manuscript?

1. Dimensions

Area of the tested solar cells

<input checked="" type="checkbox"/> Yes	Methods in the manuscript
<input type="checkbox"/> No	

Method used to determine the device area

<input checked="" type="checkbox"/> Yes	Methods in the manuscript
<input type="checkbox"/> No	

2. Current-voltage characterization

Current density-voltage (J-V) plots in both forward and backward direction

<input checked="" type="checkbox"/> Yes	Fig. 3b
<input type="checkbox"/> No	

Voltage scan conditions

For instance: scan direction, speed, dwell times

<input checked="" type="checkbox"/> Yes	Methods in main text
<input type="checkbox"/> No	

Test environment

For instance: characterization temperature, in air or in glove box

<input checked="" type="checkbox"/> Yes	Methods in main text
<input type="checkbox"/> No	

Protocol for preconditioning of the device before its characterization

<input checked="" type="checkbox"/> Yes	Methods in main text
<input type="checkbox"/> No	

Stability of the J-V characteristic

Verified with time evolution of the maximum power point or with the photocurrent at maximum power point; see ref. 7 for details.

<input checked="" type="checkbox"/> Yes	Supplementary Fig. 17, Newport certificated results
<input type="checkbox"/> No	

3. Hysteresis or any other unusual behaviour

Description of the unusual behaviour observed during the characterization

<input type="checkbox"/> Yes	Not relevant
<input checked="" type="checkbox"/> No	

Related experimental data

<input type="checkbox"/> Yes	Not relevant
<input checked="" type="checkbox"/> No	

4. Efficiency

External quantum efficiency (EQE) or incident photons to current efficiency (IPCE)

<input checked="" type="checkbox"/> Yes	Fig. 3d
<input type="checkbox"/> No	

A comparison between the integrated response under the standard reference spectrum and the response measure under the simulator

<input checked="" type="checkbox"/> Yes	In the main text
<input type="checkbox"/> No	

For tandem solar cells, the bias illumination and bias voltage used for each subcell

<input type="checkbox"/> Yes	<i>State where this information can be found in the text.</i>
<input type="checkbox"/> No	<i>Explain why this information is not reported/not relevant.</i>

5. Calibration

Light source and reference cell or sensor used for the characterization

<input checked="" type="checkbox"/> Yes	Methods in the main text
<input type="checkbox"/> No	

Confirmation that the reference cell was calibrated and certified

<input checked="" type="checkbox"/> Yes	Methods in the main text
<input type="checkbox"/> No	

Calculation of spectral mismatch between the reference cell and the devices under test	<input checked="" type="checkbox"/> Yes <input type="checkbox"/> No	It has been calibrated
6. Mask/aperture		
Size of the mask/aperture used during testing	<input checked="" type="checkbox"/> Yes <input type="checkbox"/> No	Methods in the main text
Variation of the measured short-circuit current density with the mask/aperture area	<input checked="" type="checkbox"/> Yes <input type="checkbox"/> No	Newport certification report in supplementary Fig. 17
7. Performance certification		
Identity of the independent certification laboratory that confirmed the photovoltaic performance	<input checked="" type="checkbox"/> Yes <input type="checkbox"/> No	Newport
A copy of any certificate(s) <i>Provide in Supplementary Information</i>	<input checked="" type="checkbox"/> Yes <input type="checkbox"/> No	Supplementary Fig. 17 and Fig. 18
8. Statistics		
Number of solar cells tested	<input checked="" type="checkbox"/> Yes <input type="checkbox"/> No	Supplementary Fig. 16
Statistical analysis of the device performance	<input checked="" type="checkbox"/> Yes <input type="checkbox"/> No	Supplementary Fig. 16
9. Long-term stability analysis		
Type of analysis, bias conditions and environmental conditions <i>For instance: illumination type, temperature, atmosphere humidity, encapsulation method, preconditioning temperature</i>	<input checked="" type="checkbox"/> Yes <input type="checkbox"/> No	Fig. 5 and Supplementary Fig. 24